The Astrophysical Journal, 960:29 (28pp), 2024 January 1 https://doi.org/10.3847/1538-4357/ad0153

Strong Carbon Features and a Red Early Color in the Underluminous Type Ia SN 2022xkq

Jeniveve Pearson[1], David J. Sand[1], Peter Lundqvist[2], Lluís Galbany[3,4], Jennifer E. Andrews[5], K. Azalee Bostroem[1,52], Yize Dong (董一泽)[6], Emily Hoang[6], Griffin Hosseinzadeh[1], Daryl Janzen[7], Jacob E. Jencson[8], Michael J. Lundquist[9], Darshana Mehta[6], Nicolás Meza Retamal[6], Manisha Shrestha[1], Stefano Valenti[6], Samuel Wyatt[10], Joseph P. Anderson[11,12], Chris Ashall[13], Katie Auchettl[14,15], Eddie Baron[16,17,18], Stéphane Blondin[19], Christopher R. Burns[20], Yongzhi Cai (蔡永志)[21,22,23], Ting-Wan Chen[24], Laura Chomiuk[25], David A. Coulter[15], Dane Cross[3], Kyle W. Davis[15], Thomas de Jaeger[26], James M. DerKacy[13], Dhvanil D. Desai[27], Georgios Dimitriadis[28], Aaron Do[27], Joseph R. Farah[29], Ryan J. Foley[15], Mariusz Gromadzki[30], Claudia P. Gutiérrez[3,4], Joshua Haislip[31], Jonay I. González Hernández[32,33], Jason T. Hinkle[27], Willem B. Hoogendam[27,53], D. Andrew Howell[29,34], Peter Hoeflich[35], Eric Hsiao[35], Mark E. Huber[27], Saurabh W. Jha[36], Cristina Jiménez Palau[3,4], Charles D. Kilpatrick[37], Vladimir Kouprianov[31], Sahana Kumar[38], Lindsey A. Kwok[36], Conor Larison[36], Natalie LeBaron[39], Xavier Le Saux[15], Jing Lu[25], Curtis McCully[29,34], Tycho Mera Evans[35], Peter Milne[1], Maryam Modjaz[38], Nidia Morrell[40], Tomás E. Müller-Bravo[3,4], Megan Newsome[29,34], Matt Nicholl[41], Estefania Padilla Gonzalez[29,34], Anna V. Payne[27,42], Craig Pellegrino[34,38], Kim Phan[3,4], Jonathan Pineda-García[43], Anthony L. Piro[20], Lara Piscarreta[3], Abigail Polin[20,44], Daniel E. Reichart[31], César Rojas-Bravo[15], Stuart D. Ryder[45,46], Irene Salmaso[47,48], Michaela Schwab[36], Melissa Shahbandeh[8,42], Benjamin J. Shappee[27], Matthew R. Siebert[42], Nathan Smith[1], Jay Strader[25], Kirsty Taggart[15], Giacomo Terreran[34], Samaporn Tinyanont[49], M. A. Tucker[50,51,54], Giorgio Valerin[47,48], and D. R. Young[41]

[1] Steward Observatory, University of Arizona, 933 North Cherry Avenue, Tucson, AZ 85721-0065, USA; jenivevepearson@arizona.edu
[2] Oskar Klein Centre, Department of Astronomy, Stockholm University, Albanova University Centre, SE-106 91 Stockholm, Sweden
[3] Institute of Space Sciences (ICE, CSIC), Campus UAB, Carrer de Can Magrans, s/n, E-08193 Barcelona, Spain
[4] Institut d'Estudis Espacials de Catalunya, Gran Capità, 2-4, Edifici Nexus, Desp. 201, E-08034 Barcelona, Spain
[5] Gemini Observatory, 670 North A'ohoku Place, Hilo, HI 96720-2700, USA
[6] Department of Physics and Astronomy, University of California, Davis, 1 Shields Avenue, Davis, CA 95616-5270, USA
[7] Department of Physics & Engineering Physics, University of Saskatchewan, 116 Science Place, Saskatoon, SK S7N 5E2, Canada
[8] Department of Physics and Astronomy, The Johns Hopkins University, 3400 North Charles Street, Baltimore, MD 21218, USA
[9] W. M. Keck Observatory, 65-1120 Māmalahoa Highway, Kamuela, HI 96743-8431, USA
[10] Department of Astronomy, University of Washington, 3910 15th Avenue NE, Seattle, WA 98195-0002, USA
[11] European Southern Observatory, Alonso de Córdova 3107, Casilla 19, Santiago, Chile
[12] Millennium Institute of Astrophysics MAS, Nuncio Monsenor Sotero Sanz 100, Off. 104, Providencia, Santiago, Chile
[13] Department of Physics, Virginia Tech, 850 West Campus Drive, Blacksburg, VA 24061, USA
[14] School of Physics, The University of Melbourne, Parkville, VIC 3010, Australia
[15] Department of Astronomy and Astrophysics, University of California, Santa Cruz, CA 95064-1077, USA
[16] Planetary Science Institute, 1700 East Fort Lowell Road, Suite 106, Tucson, AZ 85719-2395, USA
[17] Hamburger Sternwarte, Gojenbergsweg 112, D-21029 Hamburg, Germany
[18] Homer L. Dodge Department of Physics and Astronomy, University of Oklahoma, 440 W. Brooks, Norman, OK 73019-2061, USA
[19] Aix-Marseille Univ, CNRS, CNES, LAM, F-13388 Marseille, France
[20] Observatories of the Carnegie Institute for Science, 813 Santa Barbara Street, Pasadena, CA 91101-1232, USA
[21] Yunnan Observatories, Chinese Academy of Sciences, Kunming 650216, People's Republic of China
[22] Key Laboratory for the Structure and Evolution of Celestial Objects, Chinese Academy of Sciences, Kunming 650216, People's Republic of China
[23] International Centre of Supernovae, Yunnan Key Laboratory, Kunming 650216, People's Republic of China
[24] Graduate Institute of Astronomy, National Central University, 300 Jhongda Road, 32001 Jhongli, Taiwan
[25] Center for Data Intensive and Time Domain Astronomy, Department of Physics and Astronomy, Michigan State University, East Lansing, MI 48824, USA
[26] LPNHE, (CNRS/IN2P3, Sorbonne Université, Université Paris Cité), Laboratoire de Physique Nucléaire et de Hautes Énergies, F-75005, Paris, France
[27] Institute for Astronomy, University of Hawai'i, 2680 Woodlawn Drive, Honolulu, HI 96822-1839, USA
[28] School of Physics, Trinity College Dublin, The University of Dublin, Dublin 2, Ireland
[29] Department of Physics, University of California, Santa Barbara, CA 93106-9530, USA
[30] Astronomical Observatory, University of Warsaw, Al. Ujazdowskie 4, 00-478 Warszawa, Poland
[31] Department of Physics and Astronomy, University of North Carolina, 120 East Cameron Avenue, Chapel Hill, NC 27599, USA
[32] Instituto de Astrofísica de Canarias, E-38205 La Laguna, Tenerife, Spain
[33] Universidad de La Laguna, Dept. Astrofísica, E-38206 La Laguna, Tenerife, Spain
[34] Las Cumbres Observatory, 6740 Cortona Drive, Suite 102, Goleta, CA 93117-5575, USA
[35] Department of Physics, Florida State University, 77 Chieftan Way, Tallahassee, FL 32306-4350, USA
[36] Department of Physics and Astronomy, Rutgers, the State University of New Jersey, 136 Frelinghuysen Road, Piscataway, NJ 08854-8019, USA
[37] Center for Interdisciplinary Exploration and Research in Astrophysics and Department of Physics and Astronomy, Northwestern University, 1800 Sherman Avenue, 8th Floor, Evanston, IL 60201, USA
[38] Department of Astronomy, University of Virginia, Charlottesville, VA 22904, USA
[39] Department of Astronomy, University of California, Berkeley, CA 94720-3411, USA
[40] Las Campanas Observatory, Carnegie Observatories, Casilla 601, La Serena, Chile
[41] Astrophysics Research Centre, School of Mathematics and Physics, Queen's University Belfast, Belfast BT7 1NN, UK
[42] Space Telescope Science Institute, 3700 San Martin Drive, Baltimore, MD 21218-2410, USA
[43] Departamento de Ciencias Físicas, Facultad de Ciencias Exactas, Universidad Andrés Bello, Fernández Concha 700, Las Condes, Santiago, Chile
[44] Cahill Center for Astronomy and Astrophysics, California Institute of Technology, Mail Code 249-17, Pasadena, CA 91125, USA
[45] School of Mathematical and Physical Sciences, Macquarie University, NSW 2109, Australia
[46] Astronomy, Astrophysics and Astrophotonics Research Centre, Macquarie University, Sydney, NSW 2109, Australia

[47] INAF-Osservatorio Astronomico di Padova, Vicolo dell'Osservatorio 5, I-35122 Padova, Italy
[48] Dipartimento di Fisica e Astronomia "G. Galilei,"Università degli studi di Padova Vicolo dell'Osservatorio 3, I-35122 Padova, Italy
[49] National Astronomical Research Institute of Thailand (NARIT), Don Kaeo, Mae Rim District, Chiang Mai 50180, Thailand
[50] Department of Astronomy, The Ohio State University, 140 West 18th Avenue, Columbus, OH 43210, USA
[51] Center for Cosmology and Astroparticle Physics, The Ohio State University, 191 West Woodruff Ave, Columbus, OH 43210, USA
Received 2023 September 18; revised 2023 October 5; accepted 2023 October 6; published 2023 December 19

Abstract

We present optical, infrared, ultraviolet, and radio observations of SN 2022xkq, an underluminous fast-declining Type Ia supernova (SN Ia) in NGC 1784 ($D \approx 31$ Mpc), from <1 to 180 days after explosion. The high-cadence observations of SN 2022xkq, a photometrically transitional and spectroscopically 91bg-like SN Ia, cover the first days and weeks following explosion, which are critical to distinguishing between explosion scenarios. The early light curve of SN 2022xkq has a red early color and exhibits a flux excess that is more prominent in redder bands; this is the first time such a feature has been seen in a transitional/91bg-like SN Ia. We also present 92 optical and 19 near-infrared (NIR) spectra, beginning 0.4 days after explosion in the optical and 2.6 days after explosion in the NIR. SN 2022xkq exhibits a long-lived C I 1.0693 μm feature that persists until 5 days post-maximum. We also detect C II λ6580 in the pre-maximum optical spectra. These lines are evidence for unburnt carbon that is difficult to reconcile with the double detonation of a sub-Chandrasekhar mass white dwarf. No existing explosion model can fully explain the photometric and spectroscopic data set of SN 2022xkq, but the considerable breadth of the observations is ideal for furthering our understanding of the processes that produce faint SNe Ia.

Unified Astronomy Thesaurus concepts: Supernovae (1668); White dwarf stars (1799); Type Ia supernovae (1728)

Supporting material: data behind figure

1. Introduction

Type Ia supernovae (SNe Ia) result from the thermonuclear explosions of carbon-oxygen white dwarfs (Hoyle & Fowler 1960) and are a critical tool for measuring the expansion history of the universe, as they are standardizable candles (Phillips 1993; Hamuy et al. 1996; Guy et al. 2007; Jha et al. 2007). Despite their importance, the exact nature of the explosion mechanisms and progenitor systems of SNe Ia are still being actively investigated (see, e.g., Jha et al. 2019, for a recent review).

There are several critical observational probes of SNe Ia that shed light on the possible explosion and progenitor scenarios. Among the most promising are very early multiband and high-cadence light curves, which in a handful of well-observed cases have exhibited color-dependent excesses over a smooth power-law rise (e.g., Marion et al. 2016; Hosseinzadeh et al. 2017; Jiang et al. 2017; Miller et al. 2018; Dimitriadis et al. 2019; Shappee et al. 2019; Miller et al. 2020a; Burke et al. 2021; Jiang et al. 2021; Hosseinzadeh et al. 2022b; Ni et al. 2022; Sai et al. 2022; Hosseinzadeh et al. 2023b; Wang et al. 2023). Recent samples indicate that ~10%–30% of all SNe Ia, if observed early enough and with high cadence, would exhibit such excesses (Miller et al. 2020b; Bulla et al. 2020; Burke et al. 2022a, 2022b; Deckers et al. 2022). Notably, such early light-curve features were predicted for the single-degenerate scenario owing to the collision between the SN ejecta and a nondegenerate companion star, manifesting as a UV/blue excess that is visible for only a few days for favorable viewing angles (Kasen 2010). Similar "bump" features in the early light curve may also be attributable to an unusual distribution of radioactive ^{56}Ni (e.g., Magee & Maguire 2020; Magee et al. 2020), rapid velocity evolution of the Ca II H and K feature (Ashall et al. 2022), circumstellar medium (CSM)−ejecta interaction (e.g., Piro & Morozova 2016; Jiang et al. 2021), or a natural consequence of a sub-Chandrasekhar mass, double-detonation explosion (e.g., Polin et al. 2019). Even well-observed examples that do not exhibit an early light curve excess are important for understanding SN Ia light-curve demographics (e.g., Olling et al. 2015), and the early light curves of many subtypes, including transitional and 91bg-like SNe Ia, have not yet been explored.

Another key measurement in SNe Ia is the incidence of carbon in the early spectra. Depending on the explosion mechanism, some carbon can escape being burned during the runaway carbon fusion in a C/O white dwarf, which makes carbon a direct probe of the explosion. Several studies have focused on the C II λ6580 feature, which is seen on the red shoulder of the ubiquitous Si II λ6355 absorption feature and is detectable in ~20%–40% of spectra taken before maximum light (Parrent et al. 2011; Thomas et al. 2011; Blondin et al. 2012; Folatelli et al. 2012; Silverman & Filippenko 2012; Maguire et al. 2014; Wyatt et al. 2021). There is mounting evidence that the near-infrared (NIR) C I 1.0693 μm line is particularly strong in transitional and/or 91bg-like SNe Ia (Hsiao et al. 2015; Wyatt et al. 2021; Li et al. 2022).

The amount of carbon (or lack thereof) depends on the explosion physics and the degree of mixing. The pure-deflagration W7 model (Nomoto et al. 1984) leaves significant carbon behind in the outer ejecta, as does the violent merger model (Pakmor et al. 2012) and the pulsational-delayed-detonation models (Höflich et al. 1995). Meanwhile, delayed-detonation models have nearly complete carbon burning at normal SN Ia luminosities (Khokhlov 1991; Kasen et al. 2009), with increasing amounts of unburnt carbon remaining for fainter events (Höflich et al. 2002). Notably, sub-Chandrasekhar double-detonation models, which have been suggested to be the dominate explosion mechanism for faint SNe Ia (Blondin et al. 2017; Goldstein & Kasen 2018), leave little to no carbon

[52] LSSTC Catalyst Fellow.
[53] NSF Graduate Research Fellow.
[54] CCAPP Fellow.

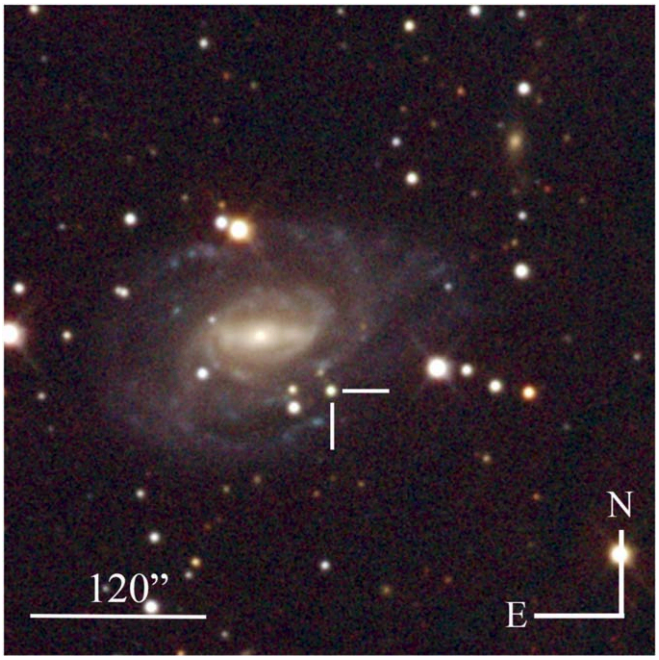

Figure 1. Composite *g*, *r*, *i* image of SN 2022xkq in NGC 1784 obtained by Las Cumbres Observatory on 2022 November 14, +18 days after *B*-band peak.

behind (e.g., Polin et al. 2019). This indicates that the presence of unburnt carbon may be a distinguishing observational signature of the explosion mechanism in faint SNe Ia.

In this paper we present high-cadence, multiwavelength photometric and spectroscopic observations of the faint SN Ia SN 2022xkq. We discuss the discovery of SN 2022xkq in Section 2, observational details in Section 3, and the proper classification for SN 2022xkq in Section 4. In Sections 5 and 6, we analyze the photometric and spectroscopic observations of SN 2022xkq and compare them to models of several different explosion scenarios. In Section 7, we examine radio observations and their constraints on the progenitor system. We discuss the possible origins of the observed color and the implications of spectral features in Section 8 and conclude in Section 9.

2. Discovery

SN 2022xkq, also known as DLT22r, was discovered at R. A. (J2000) = $05^{h}05^{m}23\overset{s}{.}710$, decl.(J2000) = $-11°52'56\overset{''}{.}10$ by the Distance Less Than 40 Mpc survey (DLT40; for survey description see Tartaglia et al. 2018) on 2022 October 13, 06:43:35 UTC (59865.28 MJD; Janzen et al. 2022). The last nondetection was on 2022 October 12, 11:47:37 UTC (2,459,864.99 JD) by the Asteroid Terrestrial-impact Last Alert System (ATLAS) to a $>2\sigma$ limit of $o > 19.47$ (Tonry et al. 2018; Smith et al. 2020; Shingles et al. 2021). SN 2022xkq was initially classified as a Type I SN (Chen et al. 2022a) and then reclassified as an SN Ic (Hosseinzadeh et al. 2022a). It was eventually classified as an SN 1991bg-like SN Ia (Chen et al. 2022b); the exact classification will be discussed further in Section 4.

As shown in Figure 1,[55] SN 2022xkq is located in NGC 1784, a barred spiral SB(r)c galaxy (de Vaucouleurs et al. 1991; Erwin & Debattista 2013) and SN 2022xkq is the first recorded SN in the galaxy. Underluminous SNe Ia preferentially explode in older galaxy populations and are most likely to be found in elliptical and occasionally in early-type spiral galaxies (Hamuy et al. 2000; Howell 2001; Gallagher et al. 2005; Sullivan et al. 2006; Li et al. 2011; Nugent et al. 2023). However, late-type spiral galaxies also possess old stellar populations, and while underluminous SNe Ia in late-type hosts are uncommon, there have been a few. The most notable is SN 1999by, which occurred in the SAb galaxy NGC 2841 (Höflich et al. 2002; Garnavich et al. 2004).

NGC 1784 has a redshift $z = 0.007735$ (Koribalski et al. 2004). The Virgo infall distance to NGC 1784 is 31 ± 2 Mpc ($\mu = 32.46 \pm 0.15$ mag; Mould et al. 2000) for $H_0 = 70$ km s^{-1} Mpc^{-1}, which we use as the distance to SN 2022xkq, and is listed in Table 1. This measurement is in general agreement with the Tully–Fisher distance of 28.07 Mpc (Tully et al. 2016) for $H_0 = 70$ km s^{-1} Mpc^{-1}, as well as the distance modulus calculated based on the multiband light curve by SNooPy (see Section 5; Burns et al. 2011) of $\mu = 32.9 \pm 0.1$ mag for $H_0 = 72$ km s^{-1} Mpc^{-1}.

Table 1
Summary of SN 2022xkq Properties

Parameter	Value
Last Nondetection	MJD 59864.49
First detection	MJD 59865.28
Explosion epoch[a]	MJD 59865.0 ± 0.3
Redshift z	0.007735
Distance	31 ± 2 Mpc
Distance modulus (μ)	32.46 ± 0.15 mag
$E(B-V)_{\rm tot}$	0.1155 ± 0.0023 mag
Peak magnitude ($B_{\rm max}$)	-18.01 ± 0.15 mag
Time of $B_{\rm max}$	MJD 59879.03 ± 0.34
$s_{\rm BV}$	0.63 ± 0.03
$\Delta m_{15}(B)$	1.65 ± 0.03 mag
^{56}Ni mass	$0.22 \pm 0.03\ M_{\odot}$
Si II velocity (−11.6 days)	$11,920 \pm 350$ km s^{-1}
Si II velocity (1.2 days)	$9,980 \pm 200$ km s^{-1}
Si II λ5972 EW (1.2 days)	38 ± 1 Å
Si II λ6355 EW (1.2 days)	129 ± 7 Å
Hα luminosity	$<8.8 \times 10^{36}$ erg s^{-1}
He I λ5875 luminosity	$<4.0 \times 10^{37}$ erg s^{-1}
He I λ6678 luminosity	$<8.8 \times 10^{36}$ erg s^{-1}
Stripped H mass (Botyánszki)	$\lesssim 2 \times 10^{-4}\ M_{\odot}$
Stripped H mass (Dessart)	$\lesssim 7 \times 10^{-5} M_{\odot}$
Stripped He mass (Botyánszki)	$\lesssim 7 \times 10^{-4}\ M_{\odot}$

Note.
[a] From power-law fit.

3. Observations and Data Reduction

3.1. Photometry

Following the discovery of SN 2022xkq by the DLT40 survey, continued photometric monitoring was done by two of DLT40's discovery telescopes, the PROMPT5 0.4 m telescope at the Cerro Tololo Inter-American Observatory and the PROMPT-USASK 0.4 m telescope at Sleaford Observatory. Observations taken by these telescopes using a Clear or Open filter (labeled DLT40 in Figure 2) are calibrated to the Sloan Digital Sky Survey *r* band, as described in Tartaglia et al. (2018). These "DLT40"-band observations were taken with a cadence of ∼9 images per day until maximum light, ∼3 per day for the next 40 days, and ∼1 per day for the following

[55] Image produced using https://afterglow.skynet.unc.edu.

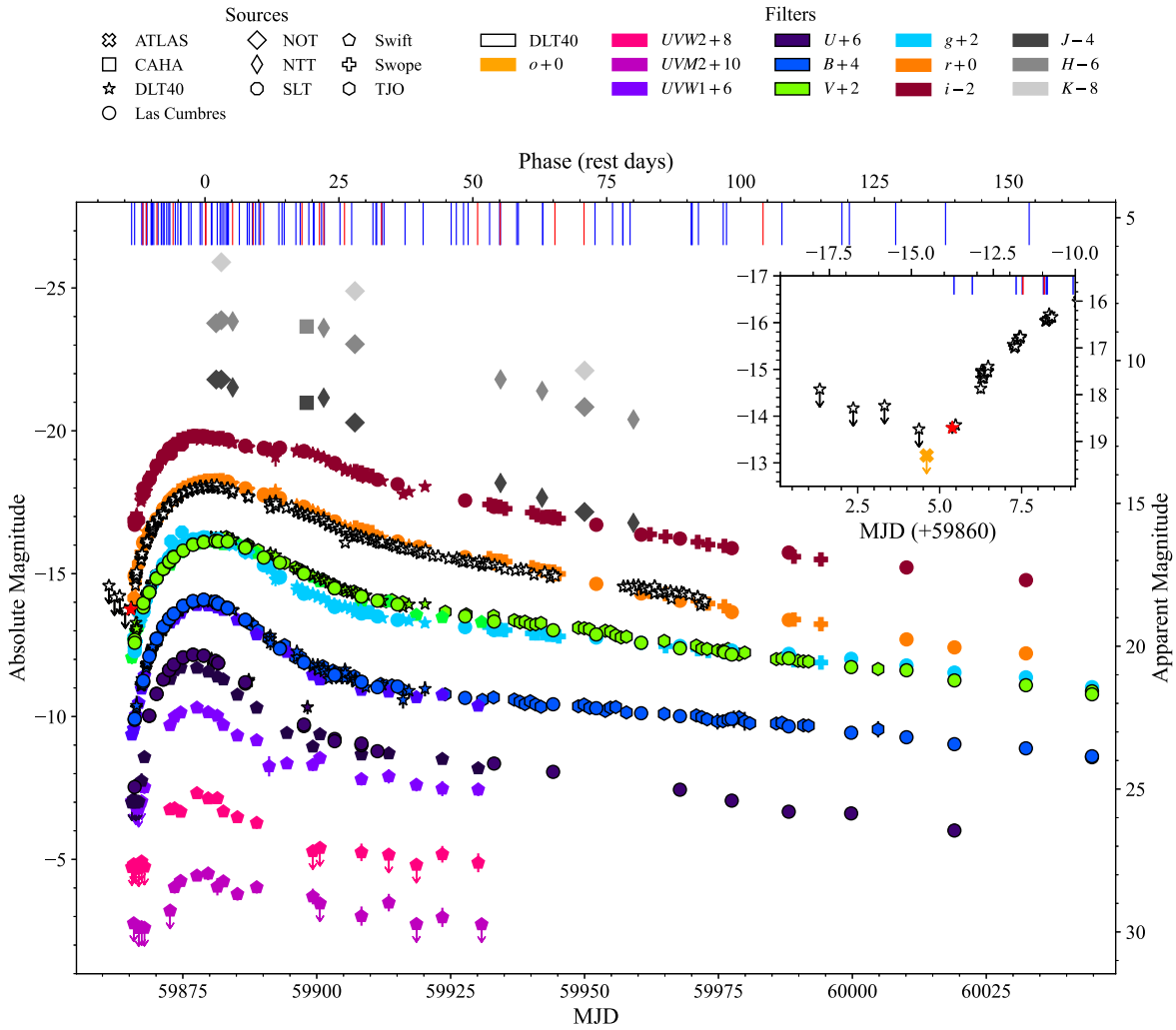

Figure 2. SN 2022xkq light curves from DLT40 (stars), Las Cumbres Observatory (circles), SLT (side-up hexagons), Swift (pentagons), Swope (plus signs), and TJO (vertex-up hexagons). NIR photometry from NTT, NOT, and CAHA is also included (quadrilaterals). Main figure: light curves with offsets in absolute and extinction-corrected apparent magnitudes. Swift observations are plotted as nondetections when the measurement error is $>3\sigma$. Inset: zoom-in of the DLT40 light curve immediately before and after discovery without offsets. The DLT40 discovery is marked by the red star, and the last nondetection by ATLAS is marked by the yellow-orange cross. Epochs of optical (blue) and infrared (red) spectra are displayed as lines along the upper x-axis. Phase is relative to the time of $B_{\rm max}$ (MJD 59879.03). (The data used to create this figure are available.)

53 days. Additionally, multiband *BVgri* photometry was taken at the Prompt5 telescope at a cadence of ∼6 observations per day until maximum light and ∼2 per day for the next 40 days. The *BVgri* light curves were created using aperture photometry and calibrating to the APASS (*BVgri*) catalog.

Further *UBVgri* photometry of SN 2022xkq was obtained using the Sinistro cameras on Las Cumbres Observatory's robotic 1 m telescopes (Brown et al. 2013), located at the Siding Spring Observatory, the South African Astronomical Observatory, and the Cerro Tololo Inter-American Observatory as part of the Global Supernova Project (GSP) collaboration. The photometric data from Las Cumbres Observatory were reduced using `lcogtsnpipe` (Valenti et al. 2016), a PyRAF-based image reduction pipeline. `lcogtsnpipe` utilizes a low-order polynomial fit and a standard point-spread function (PSF) fitting technique to remove the background and calculate instrumental magnitudes. Apparent magnitudes were calibrated to the APASS (*BVgri*) catalog and a Landolt (*U*) standard field that was observed on 2022 November 24 alongside observations of SN 2022xkq.

We also include *BV* photometry obtained with the 0.8 m Telescopi Joan Oró (TJO) at the Montsec Observatory. Instrumental magnitudes were measured using `AutoPhOT` (Brennan & Fraser 2022) and calibrated to *BV* APASS tabulated magnitudes.

We also collect images with the 0.4 m Ritchey–Chrétien Super Light Telescope (SLT) at the Lulin Observatory, Taiwan, as part of the Kinder project (Chen et al. 2021), and we use Photutils (Bradley et al. 2022) to perform aperture photometry on the images.

Additionally, we include photometric observations in *gri* bands taken with the Swope 1 m optical telescope at Las Campanas Observatory, Chile, taken as part of the Swope Supernova Survey. All Swope photometry was processed using biases and flat fields in the same instrumental configuration as described in Kilpatrick et al. (2018), using the `photpipe` imaging and photometry package (Rest et al. 2005), including bias subtraction, flat-fielding, image stitching, and photometric calibration. Observations were calibrated using standard sources from the Pan-STARRS DR1 catalog (Flewelling et al. 2020).

Using the Pan-STARRS1 3π images as templates, we performed image subtraction using `hotpants` (Becker 2015) and forced photometry at the position of SN 2022xkq to obtain the reported Swope photometric measurements.

We include *JHK* photometry obtained with SOFI mounted on the European Southern Observatory (ESO) 3.5 m New Technology Telescope (NTT) at La Silla Observatory, Omega2000 at the 3.5 m Calar Alto telescope (CAHA), and NOTCam at the 2.5 m Nordic Optical Telescope (NOT). Photometry was measured with `AutoPhOT` and calibrated to Two Micron All Sky Survey star cataloged photometry.

We also include optical and ultraviolet (UV) photometry from our high-cadence photometric follow-up campaign with the Ultraviolet/Optical Telescope (UVOT; Roming et al. 2005) on the Neil Gehrels Swift Observatory (Gehrels et al. 2004). The aperture photometry from the UVOT images was measured using the High-Energy Astrophysics software (HEA-Soft; NASA High Energy Astrophysics Science Archive Research Center (Heasarc), 2014) and a 3″ aperture centered at the position of SN 2022xkq. The background was measured from a region devoid of stars. Zero-points for the UVOT data were taken from Breeveld et al. (2011), with time-dependent sensitivity corrections updated in 2020.

The complete Milky Way and host-extinction-corrected (see Section 3.4 for details) multiband light curves of SN 2022xkq are shown in Figure 2.

3.2. Spectroscopy

We present 92 optical spectra from the first 153 days following the explosion. These spectra where observed using the Robert Stobie Spectrograph (RSS) on the Southern African Large Telescope (SALT; Smith et al. 2006), the ESO Faint Object Spectrograph and Camera (EFOSC2; Buzzoni et al. 1984) on the NTT (ESO-NTT) as part of the ePESSTO+ survey (Smartt et al. 2015), the FLOYDS spectrographs (Brown et al. 2013) on the Las Cumbres Observatory's 2 m Faulkes Telescopes North and South (FTN/FTS) as part of the GSP collaboration, the Inamori-Magellan Areal Camera and Spectrograph (IMACS; Dressler et al. 2011) on the Magellan Baade Telescope, the Alhambra Faint Object Spectrograph and Camera (ALFOSC) on the Nordic Optical Telescope (NOT), the Goodman High Throughput Spectrograph (GHTS; Clemens et al. 2004) on the Southern Astrophysical Research Telescope (SOAR), the Boller and Chivens Spectrograph (B&C) on the University of Arizona's Bok 2.3 m telescope located at Kitt Peak Observatory, the University of Hawaii 2.2 m telescope (UH88) on Maunakea using the Supernova Integral Field Spectrograph (SNIFS; Lantz et al. 2004) as part of the Spectroscopic Classification of Astronomical Transients survey (SCAT; Tucker et al. 2022), one of the Multi-Object Double Spectrographs (MODS1; Pogge et al. 2010) on the Large Binocular Telescope (LBT), the Kitt Peak National Observatory Ohio State Multi-Object Spectrograph (KOSMOS; Martini et al. 2014; Tran et al. 2019) instrument at the Astrophysical Research Consortium 3.5 m telescope (ARC) at Apache Point Observatory, the Intermediate Dispersion Spectrograph (IDS) on the Isaac Newton Telescope (INT), the Binospec instrument on the MMT (Fabricant et al. 2019), the Optical System for Imaging and low-Resolution Integrated Spectroscopy (OSIRIS; Cepa et al. 2000, 2003) at Gran Telescopio Canarias (GTC), the Kast dual-beam spectrograph (Miller & Stone 1993) on the Lick Shane 3 m telescope, the Low-Resolution Imaging Spectrograph (LRIS; Oke et al. 1995) on the 10 m Keck I telescope as part of the Young Supernova Experiment (YSE; Jones et al. 2021; Aleo et al. 2023), and the Low Dispersion Survey Spectrograph (LDSS-3; Stevenson et al. 2016) on the Magellan Clay Telescope. We also include the two classification spectra (Chen et al. 2022a, 2022b) from the Transient Name Server that were not obtained by our team. These spectra were taken by the Zwicky Transient Facility (ZTF; Bellm et al. 2019) using the Spectral Energy Distribution Machine (SEDM; Blagorodnova et al. 2018) instrument on the Palomar 60-inch telescope (P60). Optical spectra were reduced using the FLOYDS pipeline (Valenti et al. 2014), the PyNOT-redux reduction pipeline,[56] the PESSTO pipeline (Smartt et al. 2015), PySALT (Crawford et al. 2010), the Goodman pipeline (Torres et al. 2017), the IDSRED package (Müller Bravo 2023), the SNIFS reduction pipeline (Tucker et al. 2022), the Binospec IDL pipeline (Kansky et al. 2019), the modsCCDRed package (Pogge 2019), the UCSC Spectral Pipeline[57] (Siebert et al. 2019), and standard IRAF and PyRAF routines (Tody 1986; Science Software Branch at STScI 2012).

We also present 19 NIR spectra taken using the Near-Infrared Echellette Spectrometer (NIRES; Wilson et al. 2004) on Keck II as part of the Keck Infrared Transient Survey (KITS) collaboration (Tinyanont et al. 2023), the Son of ISAAC spectrograph (SOFI; Moorwood et al. 1998) on ESO-NTT, the Espectrógrafo Multiobjeto Infra-Rojo (EMIR; Garzón et al. 2022) on GTC, and TripleSpec (Schlawin et al. 2014) on the Southern Astrophysical Research Telescope (SOAR). The NIRES data were reduced using the PypeIt package (Prochaska et al. 2020b, 2020a). SOFI data were reduced using the PESSTO pipeline (Smartt et al. 2015). EMIR observations were reduced using PyEmir (Pascual et al. 2010; Cardiel et al. 2019). The Triplespec data were reduced using a modified version of the Spextool package (Cushing et al. 2004) and were corrected for telluric absorption with the software and prescription of Vacca et al. (2003).

All spectra are corrected for Milky Way extinction and the host galaxy redshift ($z = 0.007735$). Optical spectra are plotted in Figures 3 and 4, and infrared spectra are plotted in Figure 5. All spectra are logged in Table 3.

3.3. Radio Observations

SN 2022xkq was observed with the Australia Telescope Compact Array (ATCA) at 5.5 and 9.0 GHz on 2022 October 15 (12 days before $B_{\rm max}$) between 19:55 and 22:50 UT using a bandwidth of 2 GHz (Ryder et al. 2022). The observations and reductions were done in a similar way to what was described for SN 2018gv in Lundqvist et al. (2020). Since the ATCA primary flux calibrator was below the horizon throughout, PKS B0823–500 was used as the flux and bandpass calibrator, while PKS B0514–161 was observed every 15 minutes for gain and phase calibration. No radio emission was detected to 3σ upper limits on the flux density of 0.07 and 0.04 mJy at 5.5 and 9.0 GHz, respectively. For a host galaxy distance of 31 Mpc, this implies upper limits on the luminosity of 8.05 (4.60) $\times 10^{25}$ erg s^{-1} Hz^{-1} for 5.5 (9.0) GHz.

[56] https://pypi.org/project/PyNOT-redux/
[57] https://github.com/msiebert1/UCSC_spectral_pipeline

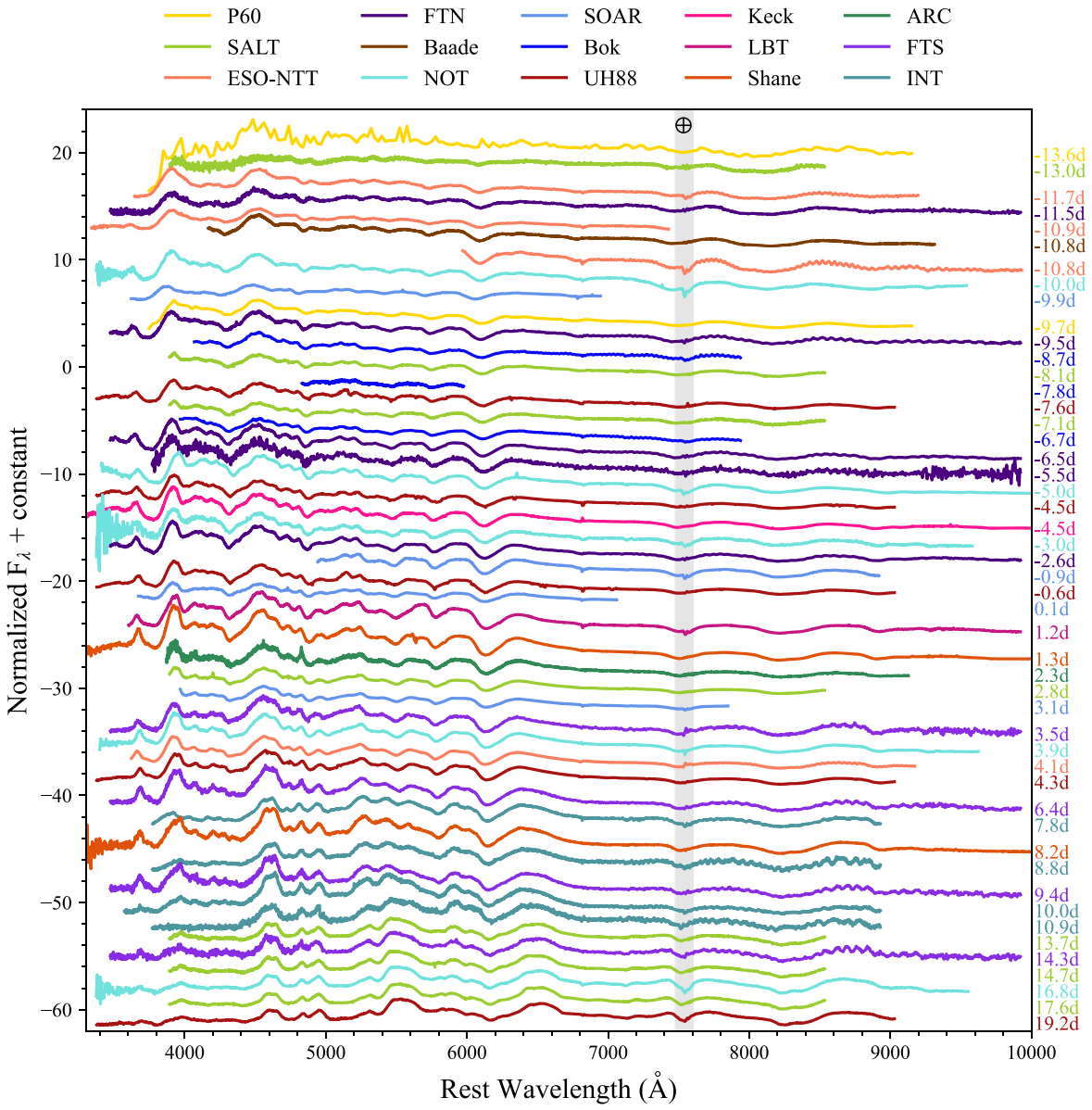

Figure 3. Optical spectroscopic evolution of SN 2022xkq until 20 days post-maximum light, corrected for $E(B-V)_{\rm tot}=0.12$. SN 2022xkq clearly exhibits the characteristic 91bg-type Ti II band from 4000 to 4500 Å (see Figure 7 for comparison to other underluminous SNe Ia). Spectra are color-coded to denote telescope (see Section 3 for more details). Labels are relative to the time of $B_{\rm max}$.

3.4. Extinction

The equivalent widths (EWs) of Na I D absorption lines correlate with interstellar dust extinction (Richmond et al. 1994; Munari & Zwitter 1997). Na I D EWs can be converted to $E(B-V)$ values using Equation (9) of Poznanski et al. (2012), with an additional normalization factor of 0.86 from Schlafly et al. (2010). However, this relation saturates at an EW of ∼0.2 Å. Milky Way Na I D lines are clearly apparent in the spectra of SN 2022xkq; however, the EWs of these lines are $\geqslant$0.5 Å for all observed spectra. We instead use the Schlafly & Finkbeiner (2011) value of $E(B-V)_{MW}=0.1155\pm0.0023$ mag. There is no evidence of host Na I D in any of the spectra of SN 2022xkq, so the host extinction is likely negligible.

We also estimate the host extinction by using the slope of the $B-V$ color from 30 to 90 days after V-band maximum (Lira 1996; Phillips et al. 1999). We employ this method, known as the Lira law, by using the procedure described in Phillips et al. (1999) and the equation

$$(B-V)_0 = E(B-V)_{\rm host} + 0.725 - 0.0118(t_V - 60). \quad (1)$$

In Figure 6, we perform a weighted least-squares fit to Equation (1), where $(B-V)_0$ is the $B-V$ color curve corrected for only Milky Way extinction and t_V is the phase with respect to V-band maximum. From this we find an unphysical $E(B-V)_{\rm host}=-0.059\pm0.009$ mag, assuming R_V of 3.1, which is consistent with zero given the known scatter of the Lira law (∼0.05 mag; Phillips et al. 1999). Given the location of the SN in the host (see Figure 1), minimal host extinction is expected. We therefore assume negligible host extinction and adopt $E(B-V)_{\rm tot}=E(B-V)_{MW}=0.116\pm0.002$ mag.

4. Classification

Underluminous SNe Ia come in a variety of subtypes, often with overlapping definitions. This is made more complex by

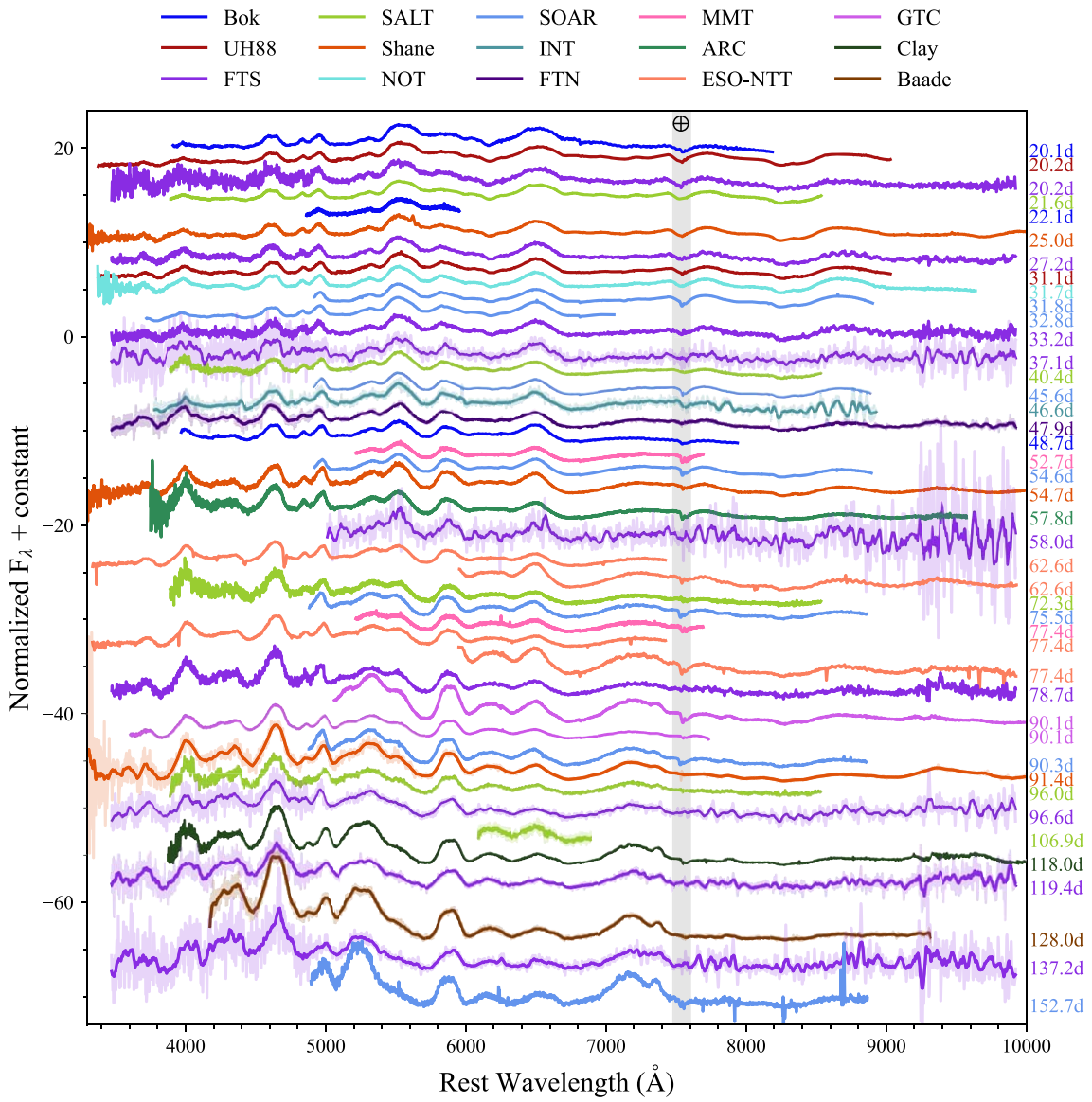

Figure 4. Same as Figure 3, but for epochs after 20 days post-maximum light. Some spectra have been rebinned for clarity; the unbinned spectra are displayed at lower opacity.

the fact that some subtype classifications are based on spectroscopy and others are based on photometry. The most common of the underluminous subtypes is 91bg-like, which make up ∼5%–20% of all SNe Ia (Graur et al. 2017; Desai et al. 2023). 91bg-like is a spectroscopic classification, characterized by strong Ti II and and Sc II features that create a distinctive "titanium trough" (Liu et al. 2023).

In contrast, "subluminous" and "transitional" are photometrically classified underluminous subtypes. Subluminous SNe have fast-declining light curves, weak or nonexistent secondary NIR maxima, and NIR peaks that occur after the *B*-band peak (Garnavich et al. 2004; Phillips 2012; Hsiao et al. 2015). Hsiao et al. (2015) suggest the existence of a photometrically classified "transitional" subtype, which bridges the gap in the Phillips (1993) relationship between between subluminous 91bg-like and normal SNe Ia. Transitional SNe Ia have fast-declining light curves similar to subluminous SNe but have a primary NIR (*iYJHK*) maximum before *B*-band maximum like normal SNe Ia.

The majority of 91bg-like SNe are subluminous (e.g., SN 1991bg and SN 1999by), and the terms 91bg-like and subluminous are often mistakenly used interchangeably. Conversely, many transitional SNe Ia (e.g., iPTF 13ebh and SN 2015bp) do not possess a Ti II trough and are not spectroscopically 91bg-like (see Figure 7). However, since transitional is a photometric classification and 91bg-like is a spectroscopic classification, these classes are not entirely separate populations.

Objects with both 91bg-like and transitional characteristics are not uncommon. Further investigation into the infrared properties of 91bg-like SNe reveals that this population is bimodal in that some 91bg-like SNe display the NIR properties of subluminous SNe while others display those of transitional SNe (Krisciunas et al. 2009; Folatelli et al. 2010; Phillips 2012; Hsiao et al. 2015; Dhawan et al. 2017). These SNe tend to be slightly brighter than subluminous 91bg-like SNe and have weaker Ti II features, though the feature is still a prominent trough shape (Dhawan et al. 2017; see Figure 7). Notable

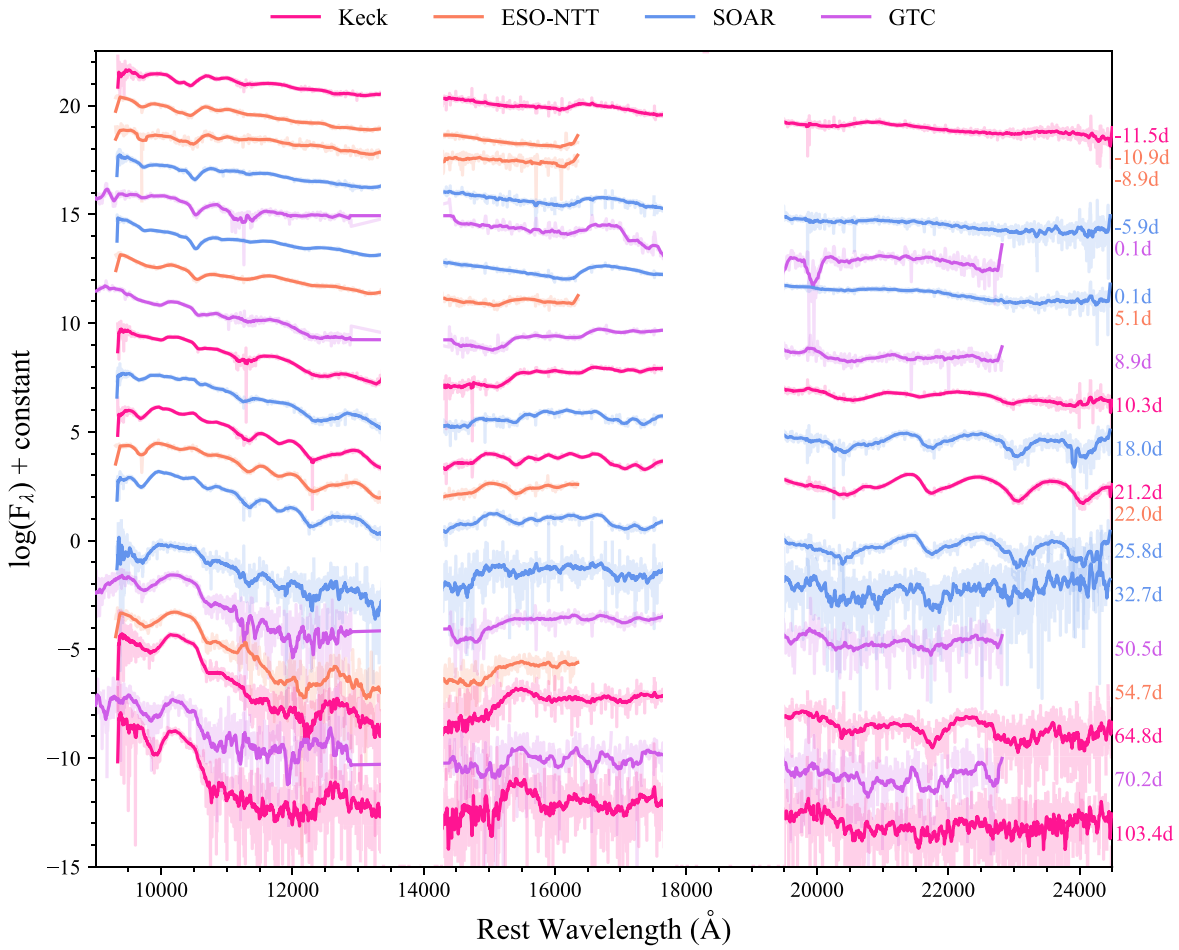

Figure 5. NIR spectroscopic evolution of SN 2022xkq, corrected for $E(B-V)_{\rm tot}=0.12$. Labels are relative to the time of $B_{\rm max}$. Spectra have been rebinned and telluric bands have been removed for clarity; the unbinned spectra are displayed at lower opacity.

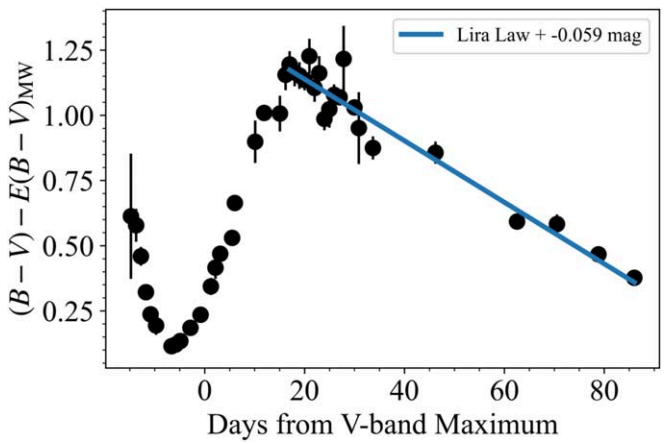

Figure 6. Milky Way extinction-corrected $B-V$ color curve of SN 2022xkq. The color on the radioactive tail is offset from the Lira (1996) law by $E(B-V)_{\rm host}=-0.059\pm0.009$ mag, which is consistent with zero given the known scatter of the Lira law. We discuss the color curve of SN 2022xkq and compare to other SNe Ia in Section 5 and Figure 9.

examples include SN 1986G (Phillips et al. 1987), SN 2003gs (Krisciunas et al. 2009), and SN 2012ij (Li et al. 2022), all of which would be spectroscopically classified as 91bg-like and photometrically classified as transitional.

As shown in Figure 7, SN 2022xkq has a strong Ti II trough (4000–4500 Å) at $B_{\rm max}$, leading to the classification of SN 2022xkq as a 91bg-like SN Ia. The shape of this titanium trough is strikingly similar to SN 1986G, which is notably photometrically transitional (Ashall et al. 2016). Similarly, SN 2022xkq exhibits all the photometric characteristics of transitional SNe (see Section 5). With a $B_{\rm max}=-18.01$ mag, SN 2022xkq is somewhat faint but still within the expected luminosity range of transitional SNe Ia. Furthermore, SN 2022xkq is a fast decliner, $\Delta m_{15}(B)=1.65\pm0.03$, similar to other SNe Ia with comparable peak magnitudes.

To determine whether SN 2022xkq has the NIR properties of the transitional subclass, we fit the *i*-band light curve. We exclude the *JHK* observations from this analysis since these observations began after NIR maximum. We find that the DLT40 and Las Cumbres Observatory *i*-band light curves peak at -1.2 ± 0.1 days and -1.0 ± 0.2 days with respect to *B*-band maximum, respectively. Given that these measurements are consistent with one another, the *i*-band peak occurs ∼1 day before the *B*-band peak, as shown in Figure 8. Further, the *i*-band light curve displays a clear secondary peak (the *r* band also displays a weak secondary peak as seen in Figure 8). Indeed, the early NIR maximum and clear secondary bump in the *i* band classify SN 2022xkq as a transitional SN Ia.

Given the strong titanium trough and early NIR maximum, we classify SN 2022xkq as spectroscopically 91bg-like and photometrically transitional. SN 2022xkq adds to the growing sample of SNe with such properties, which link purely transitional SNe and subluminous 91bg-like SNe. The photometric and spectroscopic

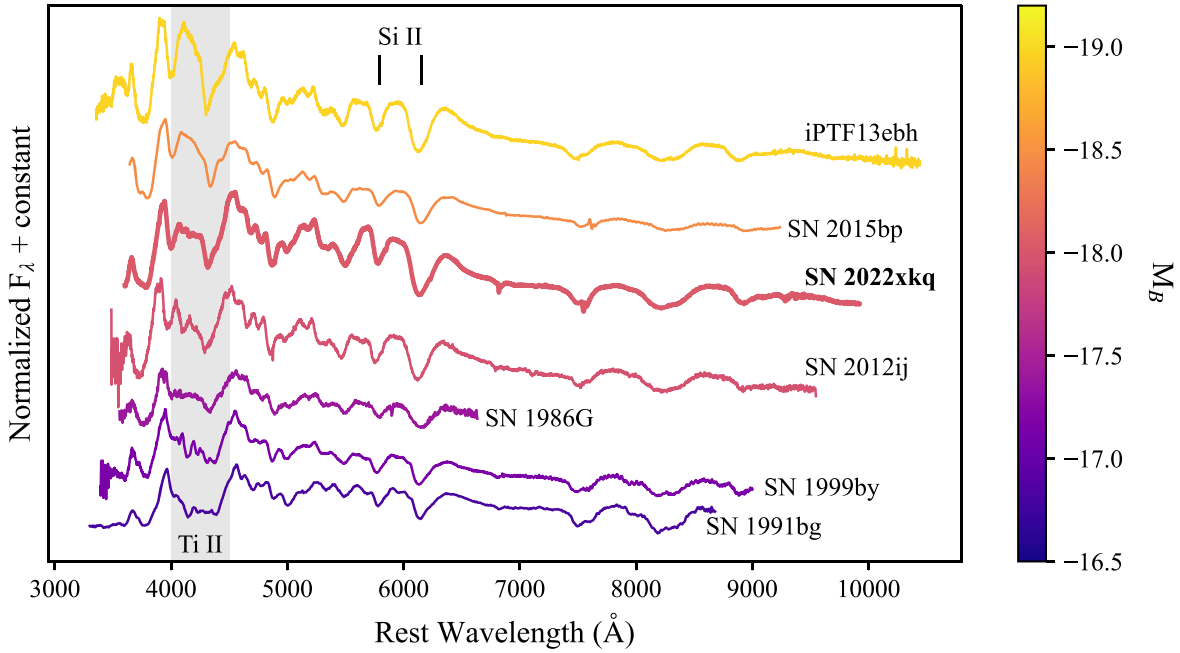

Figure 7. Comparison of spectra taken near B_{max} for transitional and 91bg-like SNe Ia. SN 2022xkq is underluminous ($B_{max} = -18.01$) and exhibits a "titanium trough" (highlighted), characteristics of 91bg-like SNe Ia. Note that the blue part of the titanium trough is actually Sc II.

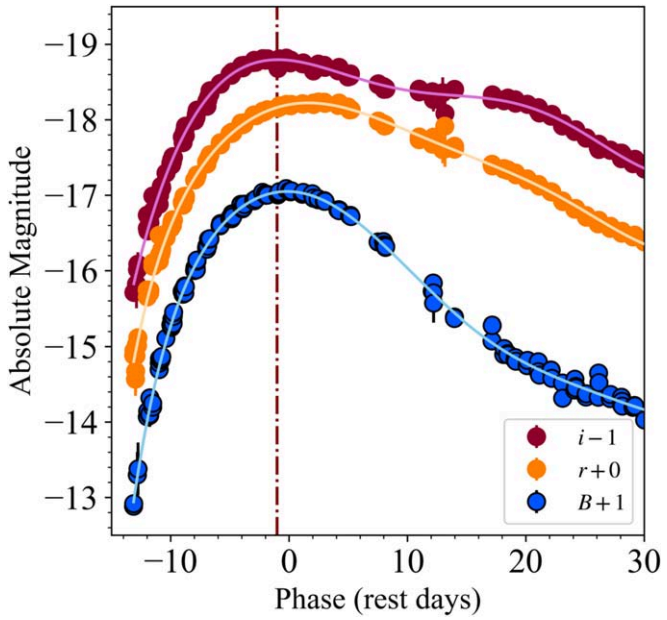

Figure 8. Plot of the *B*-, *r*-, and *i*-band DLT40 and Las Cumbres Observatory light curves of SN 2022xkq. The solid lines are polynomial fits to each band of the light curve. The maroon vertical dashed–dotted line marks the time of *i*-band maximum. The *i* band peaks at ~ -1 day relative to B_{max} and also exhibits a clear secondary maximum. The secondary maximum is also present in *r* band, though much weaker. These light-curve attributes are typical of transitional SNe Ia.

data set presented in this work makes SN 2022xkq the best-observed SN of this type and can provide insight into the different progenitor scenarios for both 91bg-like and transitional SNe.

5. Photometric Properties

Optical and Swift UV light curves (shown in Figure 2) were obtained for SN 2022xkq beginning immediately following the discovery of the SN (MJD 59865.28; 14 days before B_{max}).

Light-curve properties were fit using the `SNooPy` software package (with $H_0 = 72$ km s^{-1} Mpc^{-1}; Burns et al. 2011). Currently, `SNooPy` lacks UV templates for SN Ia fitting; thus, we exclude any UV data from these fits and only include DLT40 and Las Cumbres Observatory *BVgri* data. The results of these processes are tabulated in Table 1. SN 2022xkq reached $B_{max} = -18.01 \pm 0.15$ mag ($m_B = 14.45$ mag) on MJD 59879.03 ± 0.34. Further, SNooPy measures a decline rate of $\Delta m_{15} = 1.62 \pm 0.06$ mag and a color-stretch parameter of $s_{BV} = 0.63 \pm 0.03$. The color-stretch parameter is a better characterization of the light curves of fast-declining SNe Ia. The *B* band declines very quickly in many faint SNe, resulting in a diverging M_B versus Δm_{15} relation (Burns et al. 2014). In contrast, using the s_{BV} color-stretch parameter allows these fast-declining events to appear as part of the tail end of the normal SN Ia population (Burns et al. 2018; Gall et al. 2018). We also measure $\Delta m_{15}(B)$ directly from the DLT40 and Las Cumbres Observatory *B*-band light curve by fitting an eight-degree polynomial to the data between maximum light at 15 days post-maximum light using a least-squares method; this returns a value of 1.65 ± 0.03 (reported in Table 1). The measured Δm_{15} and s_{BV} values for SN 2022xkq are consistent with other 91bg-like and transitional SNe Ia with similar maximum M_B magnitudes.

At maximum light, the bolometric luminosity of an SN Ia is related to the amount of ^{56}Ni produced in the explosion; this relation is known as Arnett's rule (Arnett 1982; Arnett et al. 1985). To determine the ^{56}Ni mass, we use Equation (7) of Stritzinger & Leibundgut (2005), which gives the peak luminosity of an SN Ia with 1.0 $M_\odot$ of ^{56}Ni as

$$L_{max} = (2.0 \pm 0.3) \times 10^{43} \frac{M_{Ni}}{M_\odot} \text{ erg s}^{-1}, \quad (2)$$

where M_{Ni} is the nickel mass and L_{max} is the maximum bolometric luminosity. The complete bolometric light curve, which includes the *JHK* photometry, has a peak luminosity of 4.3×10^{42} erg s^{-1}, resulting in a ^{56}Ni mass of 0.22 ± 0.03 $M_\odot$.

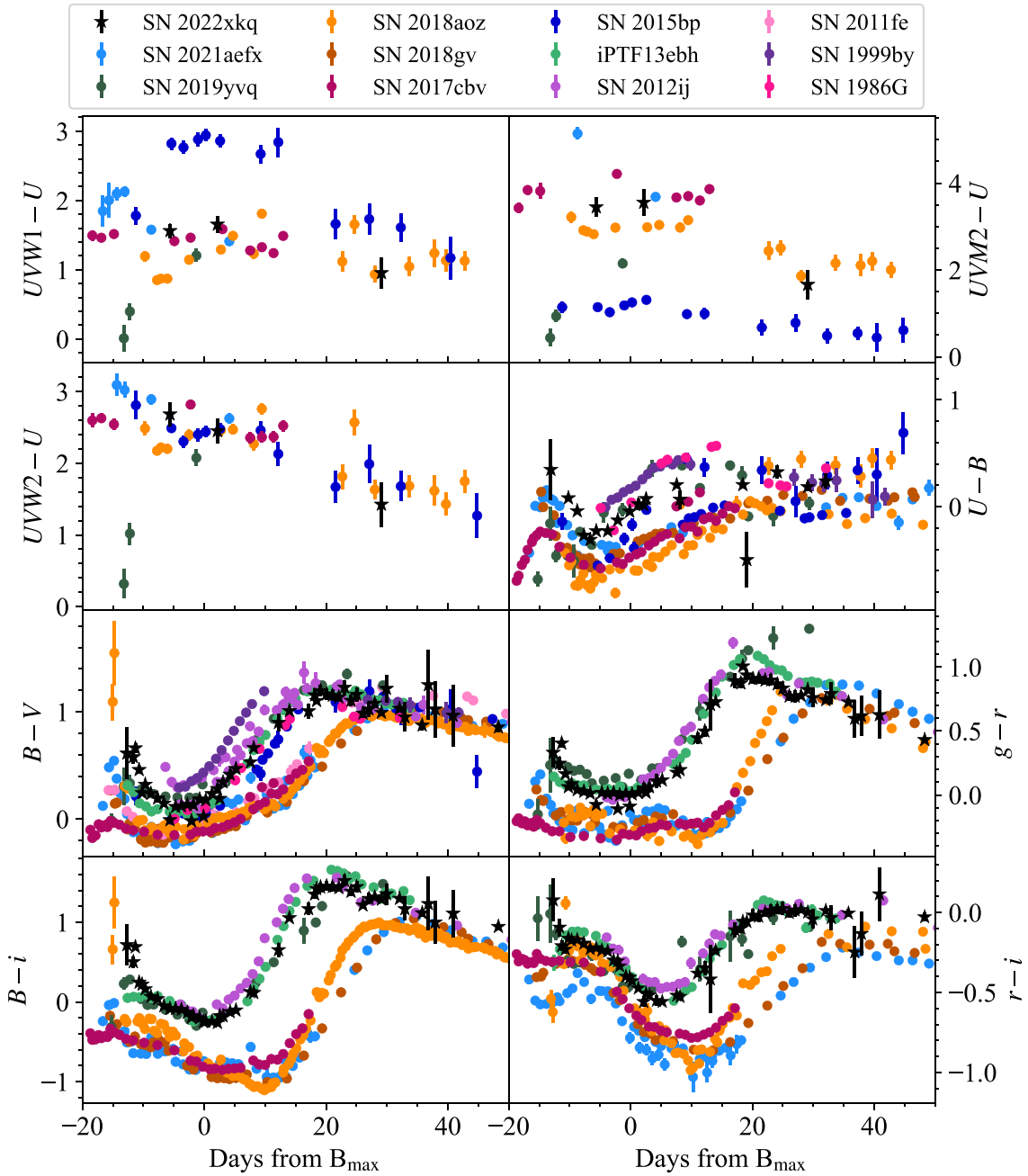

Figure 9. Color evolution of SN 2022xkq compared to other notable SNe Ia, including SN 1986G (Phillips et al. 1987), SN 1999by (Garnavich et al. 2004), SN 2011fe (Richmond & Smith 2012), SN 2012ij (Li et al. 2022), iPTF 13ebh (Hsiao et al. 2015), SN 2018aoz (Ni et al. 2022), and SN 2021aefx (Hosseinzadeh et al. 2022b). The color curve of SN 2022xkq is remarkably similar to that of SN 1986G. SN 2022xkq exhibits an early red color, which is most visible in $(B - i)$. This early red color before maximum light is most similar to that observed in SN 2018aoz, which has a bump that coincides with its early red evolution. However, SN 2022xkq is generally redder than SN 2018aoz and has a different color evolution at later times.

To ensure that this mass is reasonable, we also determine the ^{56}Ni mass from the maximum of the pseudo-bolometric light curve that we calculated from the *UBVgri* Las Cumbres Observatory light curve. To account for the ∼10% of light at maximum that is emitted outside of the optical (Suntzeff 1996), we follow the procedure in Stritzinger et al. (2006), which multiplies the resulting mass by a factor of 1.1. This method results in a pseudo-bolometric luminosity of 3.9×10^{42} erg s^{-1} and a ^{56}Ni mass of 0.21 ± 0.03 $M_{\odot}$. This mass is consistent with the value from the full bolometric light curve, so we assume that ^{56}Ni mass and list it in Table 1.

In Figure 9, we compare the color evolution of SN 2022xkq with that of notable and relevant SNe Ia: SN 1986G (Phillips et al. 1987), SN 1999by (Garnavich et al. 2004), SN 2011fe (Richmond & Smith 2012), SN 2012ij (Li et al. 2022), iPTF 13ebh (Hsiao et al. 2015), SN 2015bp (Srivastav et al. 2017), SN 2017cbv (Hosseinzadeh et al. 2017), SN 2018gv (Yang et al. 2020), SN 2018aoz (Ni et al. 2022), SN 2019yvq (Burke et al. 2021), and SN 2021aefx (Hosseinzadeh et al. 2022b). The color

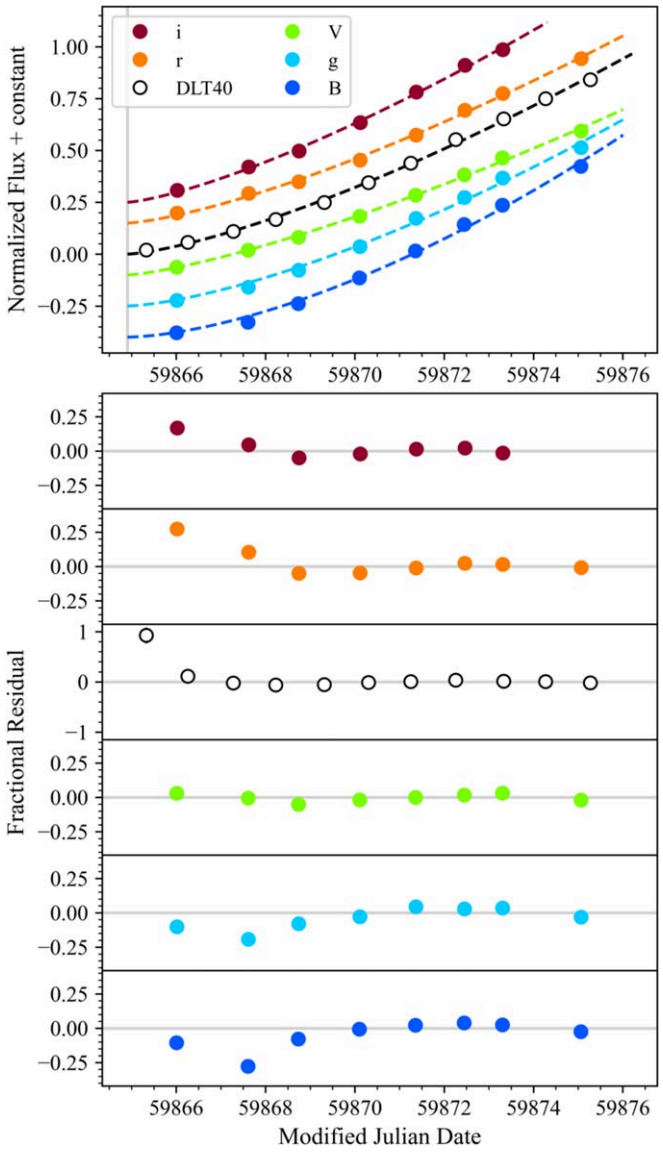

Figure 10. The binned LCO multiband and DLT40 open band light curves fit to a power law, with $t_{exp} = 59865.0 \pm 0.3$ MJD (marked by the gray line in the top panel). Residuals for each band are plotted as fractional residuals, i.e., residual divided by the power-law model flux. Immediately following explosion, the power-law fit overpredicts flux in the blue filters and underpredicts flux in the red; this indicates the presence of a slight red flux excess.

evolution of SN 2022xkq is very similar to that of the transitional SNe Ia iPTF 13ebh and SN 2015bp but also to that of SN 2012ij and SN 1986G. SN 1986G is heavily extincted, and we use $E(B-V)_{tot} = 0.88$ from Ashall et al. (2018), though $E(B-V)$ values as high as 1.1 (Cristiani et al. 1992) and as low as 0.63 (di Serego-Alighieri & Ponz 1987) have also been suggested. If we assume that SN 1986G has a slightly lower extinction (∼0.78), the color evolution of SN 1986G is almost identical to that of SN 2022xkq. The similarity in color between SN 2022xkq and SN 1986G is particularly of note because these two SNe are also remarkably similar spectroscopically.

A striking aspect of SN 2022xkq's color evolution is its very red color immediately following explosion (until ~ -10 days before the time of B_{max}), which is especially notable in the $(B-i)$ color curve, though it is present in all bands. The strong red color is somewhat similar to that observed in SN 2018aoz (Ni et al. 2022, 2023a). However, SN 2022xkq is generally redder than SN 2018aoz, and there is no bright bump in SN 2022xkq as was observed in the very early light curve of SN 2018aoz. The flux excess of SN 2022xkq is similar to the normal SNe Ia ZTF 18aayjvve and ZTF 18abdfwur (see Figure 6 in Deckers et al. 2022), which have been identified as having early red colors. Underluminous SNe Ia are intrinsically redder than normal SNe Ia (Taubenberger et al. 2008), and to our knowledge there is no 91bg-like SN Ia with multiband photometry as early as for SN 2022xkq. Therefore, this very early (within ∼5 days of explosion) red color could be typical for the subclass. The possible causes of this color will be further discussed in Section 8.1.

5.1. Power-law Fit

Densely sampled early light curves, like those obtained for SN 2022xkq, provide useful constraints on the progenitor system and/or explosion mechanism. In particular, bumps and excesses in the early light curve can be distinguishing factors among various explosion mechanisms or progenitor scenarios. Some light-curve excesses and smaller bumps can be difficult to distinguish by eye, but these features are notable when the observed light curves are compared to a power-law rise (Dimitriadis et al. 2019).

Using the nonlinear least-squares method, we fit the first 10 days of the Las Cumbres Observatory multiband and the DLT40 band (see Section 3.1 for more information) light curve to a power law of the form

$$F = c(t - t_{exp})^a , \quad (3)$$

where t_{exp} is the time of explosion, F is the flux, and c and a are free parameters. Photometry is binned to 0.3 days to reduce the impact of the different observational sites. When we limit the fit to only when the light curve reaches half-maximum flux (the procedure used in Firth et al. 2015), the unconstrained fit returns an explosion epoch that is inconsistent with the observations. Alternatively, we constrain t_{exp} to vary only between the last nondetection and discovery epoch, though an unconstrained fit of the first 10 days returns a weighted mean t_{exp} value consistent with the observed limits. When each individual filter is fit separately, a weighted mean of $t_{exp} = 59864.9 \pm 0.2$ MJD is returned, shown in Figure 10. We use this value as the explosion epoch for SN 2022xkq.

The power-law model favors $a = 1.6 \pm 0.2$ in B band and $a \sim 1.4$ in all others. This differs from the $a = 2$ of the fireball model, which is commonly used to describe the rising light curves of SNe Ia (Riess et al. 1999; Goldhaber et al. 2001). Fixing $a = 2$ results in t_{exp} almost 2 days before the last nondetection and is unable to reproduce the shape of the first few days of the rising light curve. Surveys have found $a = 2$ to be roughly consistent with normal SNe Ia (Conley et al. 2006; Hayden et al. 2010; Ganeshalingam et al. 2011; Zheng et al. 2017; Miller et al. 2020b; Fausnaugh et al. 2023); however, those with low s_{BV} ($s_{BV} < 0.8$) have been observed to have systematically lower a values than normal SNe Ia (González-Gaitán et al. 2012), so a value <2 is expected for SN 2022xkq.

There is a trend in the residuals of the power-law fit; such trends have been linked to early-time light-curve excesses (Burke et al. 2022b; Ni et al. 2022, 2023b). To best highlight the flux excess, we plot the residual as a fraction of the power-law model flux at each epoch (see lower panels of Figure 10).

Table 2
Companion-shocking Model Parameters

Parameter	Variable	Prior Shape	Prior Parameters[a]	Best-fit Value[b]	Units	
Companion-shocking Model (Kasen 2010)						
Explosion time	t_0	Uniform	59864.49	59865.28	$59864.7^{+0.3}_{-0.2}$	MJD
Binary separation	a	Uniform	0	0.1	$0.04^{+0.02}_{-0.01}$	10^{13} cm
Viewing angle	θ	Uniform	0	180	50±30	°
SiFTO Model (Conley et al. 2008)						
Time of B maximum	$t_{\max}$	Uniform	59877.14	59881.14	59879.26±0.07	MJD
Stretch	s	Log-uniform	0.5	2	0.858±0.008	dimensionless
Time shift in U	Δt_U	Gaussian	0	1	+0.14±0.07	d
Time shift in i	Δt_i	Gaussian	0	1	+0.46±0.06	d
Combined Model						
Intrinsic scatter	σ	Half-Gaussian	0	1	7.3±0.3	dimensionless

Notes.
[a] The "Prior Parameters" column lists the minimum and maximum for a uniform distribution and the mean and standard deviation for a Gaussian distribution.
[b] The "Best-fit Value" column is determined from the 16th, 50th, and 84th percentiles of the posterior distribution, i.e., median ± 1σ.

The observed residual trends indicate that the power-law fit overpredicts flux in the blue filters and underpredicts flux in the red. This red flux excess is coincident with the early red colors of SN 2022xkq.

5.2. Comparison to Models

The trend in the residual of the power-law fit is an indicator of an excess of flux in the early light curve ($\lesssim$3 days after inferred explosion). Here we compare to specific models that display early bumps and excesses to examine the possible source of this flux.

5.2.1. Companion Shocking

Early light-curve excesses may arise from SN ejecta colliding with a nondegenerate companion, resulting in the SN becoming briefly bluer and more luminous (Kasen 2010). We fit a combination of the Kasen (2010) companion-shocking component and SiFTO templates (Conley et al. 2008) using a Markov Chain Monte Carlo routine implemented in the Light Curve Fitting (Hosseinzadeh & Gomez 2020; Hosseinzadeh et al. 2023a) package using the same parameters and procedure as described in Hosseinzadeh et al. (2023b). The SiFTO models are scaled to each band so that they match the observed maximum for SN 2022xkq without preserving the colors of the original SiFTO template. The SiFTO models for U and i bands have also been slightly shifted in time when necessary to best match the observed light curve. We only include the data up to the time of $B_{\max}$ (59879.14 MJD) in the fit since the SiFTO template does not match the observed post-maximum light well, especially the secondary infrared maximum. All SN 2022xkq optical photometry is binned by 0.1 days. The SiFTO template does not include the UV, so we exclude the Swift photometry. Finally, we include a σ term that allows for proper handling of the intrinsic scatter in the photometry by effectively inflating the photometric uncertainties by a factor of $\sqrt{1+\sigma^2}$. The prior and posterior distributions of the fit parameters are given in Table 2, and the best-fit model and SiFTO templates are compared to the observed light curve in the left panel of Figure 11.

The possibility of an early excess is further justified by a comparison to a SiFTO SN Ia template (Conley et al. 2008), which fits U, B, V, and g well but underestimates the light curve in the redder bands, most notably in the i band. The companion-shocking component fits excesses that exist primarily in bluer bands. The red color of the excess in SN 2022xkq is not well explained by these models. However, the redder color of SN 2022xkq's light curve does not necessarily exclude the possibility of companion interaction (Deckers et al. 2022). Further modeling is needed to determine whether companion interaction can produce a red color without producing a detectable bump in bluer optical bands.

5.2.2. Double Detonation

Another scenario that could result in early excess flux is the double detonation of a sub-Chandrasekhar mass white dwarf. Double detonation occurs when a shell of surface helium detonates before the white dwarf core ignites. This process has been suggested as an explosion mechanism for producing underluminous SNe Ia (Polin et al. 2019; Gronow et al. 2021). Further, double-detonation models are linked to early red excesses in SNe Ia (Jiang et al. 2017; Ni et al. 2023a; see Section 8.1 for further discussion). We compare the Polin et al. (2019) double-detonation models to the observations of SN 2022xkq. To account for uncertainties in explosion time, we apply a time offset from 0 to 3 days at 0.5-day intervals. We calculate the reduced χ^2 ($\bar{\chi}^2 \equiv \chi^2/N$, where N is the number of photometric points that overlap the model) for each model in the grid. The model with the lowest $\bar{\chi}^2$ (see the right panel of Figure 11) is of a 0.9 $M_\odot$ white dwarf with a 0.05 $M_\odot$ helium shell offset by 3.0 days.

The double-detonation model can somewhat reproduce the photometry near and after maximum light in all bands except U, where the model underpredicts the luminosity. However, it fails to reproduce the color and early light curve and requires a large time shift, which is inconsistent with observed nondetections. To determine whether this was a result of comparing to the photometry rather than the color evolution, we also run the same process to find the model with light curves closest to the observed $U-B$ and $B-V$ color. The model best matched to the color is a

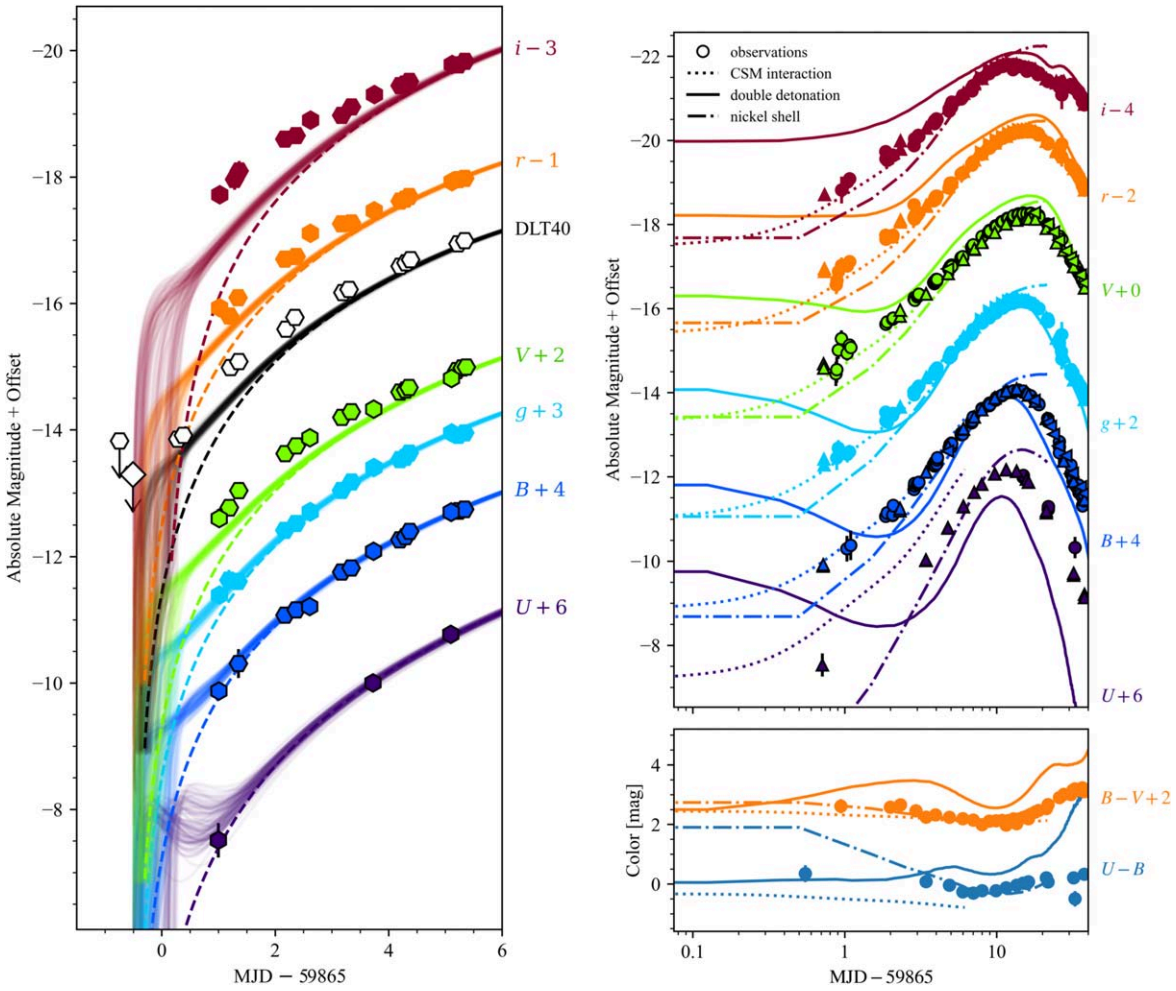

Figure 11. Left: SiFTO templates (dashed) and the combination of the SiFTO templates and Kasen (2010) companion-shocking component (solid lines) fit using the Light Curve Fitting package. A companion-shocking component is unable to reproduce the light curve in the redder bands without introducing a large blue excess, which is not observed. In combination with the residuals from the power-law fit (see Figure 10), this suggests the existence of a red excess in the early light curve. Right: the double-detonation model (solid lines) from Polin et al. (2019), nickel distribution model (dashed–dotted lines) from Magee et al. (2020), and CSM interaction model (dotted lines) from Piro & Morozova (2016), which best match the observed photometry of SN 2022xkq. No model is a particularly good description of the observed light curve, though the nickel distribution and CSM interaction models do somewhat reproduce the rising light curve, particularly in the redder bands.

1.0 $M_\odot$ white dwarf with a 0.1 $M_\odot$ helium shell offset by 3.0 days. This model is overluminous in all bands while still requiring a time shift that conflicts with nondetections.

The Polin et al. (2019) double-detonation models were not designed for SN 2022xkq; adjusting any number of parameters in the model could result in a double-detonation model that is a better match to SN 2022xkq. Specifically, we note that the next-best match to the photometry is a model of a 0.9 $M_\odot$ white dwarf with a 0.01 $M_\odot$ helium shell. The available model grid does not include any models of 0.9 $M_\odot$ white dwarfs with helium shell masses between 0.05 and 0.01 $M_\odot$, which may produce a better match to SN 2022xkq. Further, double detonation is an asymmetric process, and the viewing angle can have a significant impact on the light curve, particularly in the bluer bands (Shen et al. 2021b). The Polin et al. (2019) models are 1D and cannot account for viewing angle effects. We are therefore unable to rule out the possibility of a double-detonation scenario using the early light curves alone.

5.2.3. Distribution of Nickel

Another possible explanation for the red color in the early light curve of SN 2022xkq is shells or clumps of ^{56}Ni near the surface of the ejecta, providing extra photons in the rising light curve as a result of radioactive decay. We compare the observed color curves of SN 2022xkq to nickel models from Magee et al. (2020) and Magee & Maguire (2020), which were produced to explain the early excesses in SN 2017cbv and SN 2018oh (see dashed lines in the right panel of Figure 11). Following the same process as for the double-detonation models, we find the best-matched nickel model to be 0.4 $M_\odot$ of ^{56}Ni distributed according to an exponential density profile with a scaling parameter of 9.7 and a kinetic energy of 5.04×10^{50} erg; the model is offset by 3.0 days. This model is a good match to the observed $B - V$ color and the $U - B$ color after the first few days. Overall, the nickel models are a much better match to the observed light curve than the best double-detonation model, though the nickel model underpredicts the rising light curve and slightly overpredicts the peak luminosity in all bands. Similar to the double-detonation models, the nickel models to which we compare were not designed for SN 2022xkq and presumably could be improved to produce a better match to the observations.

5.2.4. Interaction with Circumstellar Medium

Accretion or merging proceses are integral to the production of SNe Ia, and these processes could result in CSM near an

exploding white dwarf. This ejecta–CSM interaction can result in excesses in the early light curve similar to those observed in companion-shocking models. We compare the photometry of SN 2022xkq with models of interaction with CSM from Piro & Morozova (2016) using the same procedure as for the double-detonation and nickel models. The best-matching model is of a 1.25 $M_\odot$ C/O white dwarf with 0.5 $M_\odot$ of ^{56}Ni that has been distributed using boxcar averaging of width 0.1 $M_\odot$ (for details see Piro & Morozova 2016) interacting with extended CSM material of radius 10^{11} cm and a mass of 0.3 $M_\odot$. As shown in the right panel of Figure 11, this model provides the best match to photometry of any considered model in the *BgVri* bands and is a great match to the observed $B-V$ color. However, the CSM interaction model significantly exceeds the observed *U*-band flux, resulting in a poor match to the $U-B$ color. The model also slightly undershoots the *r* and *i* bands in the epochs where the red early color is most obvious (∼3 days after explosion). The models presented in Piro & Morozova (2016) primarily produce light curves with blue early colors and flux excesses. However, these models do not consider radiative transfer and opacity effects in detail and are not expected to describe real SNe. While CSM signatures may be present in the early light curves of SNe Ia, the primary observational signature of this interaction is the presence of hydrogen in nebular spectra (see Section 6.4). A more detailed modeling of ejecta–CSM interaction in SN 2022xkq, particularly once late-time (>300 days) nebular spectra are available, may be able to better describe the rising light curve and $U-B$ color.

5.2.5. Other Possible Scenarios

Additionally, we compare the photometry of SN 2022xkq with models of pulsational-delayed detonations from Dessart et al. (2014) using the previously discussed procedure. The pulsational-delayed-detonation model set produces the worst match to the light curve of SN 2022xkq of any of the previously discussed models, and we refrain from discussing it further.

We further compare to the light curves of the delayed detonation of a Chandrasekhar white dwarf, the violent merger of two sub-Chandrasekhar white dwarfs, the detonation of a bare sub-Chandrasekhar white dwarf, and two pure-deflagration models presented in Noebauer et al. (2017). The majority of these models have red colors at early times (merger, sub-Chandrasekhar detonation, and delayed detonation). While the shape of the early light curve is somewhat similar to the violent merger model, none of these models produce a $B-V$ color evolution similar to what was observed in SN 2022xkq.

Here we briefly summarize our observations of the early light curve and our model exploration. The $B-V$ color of SN 2022xkq reveals an early color that is generally redder than most of the SNe Ia to which we compare. This color evolution is somewhat similar to the evolution observed for SN 2018aoz, which has an identified red excess. Further, the early light curve of SN 2022xkq exhibits a red excess in the residual when the light curve is fit using a simple power-law rise. The power-law residuals, combined with the SN's early color, suggest the presence of a red early excess in SN 2022xkq. To determine the mechanism responsible for this excess, we compare to several models of SN Ia explosions. However, the rising light curve and color evolution of SN 2022xkq are not well described by any of the models we consider here, though we are unable to rule out any of the mechanisms to which we compare, as tailored models may produce better results.

6. Spectroscopic Properties

6.1. Optical Spectra

As is typical of SNe Ia, the optical spectra of SN 2022xkq lack hydrogen and helium features while exhibiting characteristic strong absorption features of intermediate-mass and iron-peak elements such as Si II, Ca II, and Fe II, as seen in Figures 3 and 4.

In Figure 7, we compare an optical spectrum of SN 2022xkq taken near $B_{\max}$ to the peak spectra of other notable low-luminosity SNe Ia: the transitional iPTF 13ebh (Hsiao et al. 2015), SN 2015bp (Wyatt et al. 2021), the 91bg-like SN 1991bg (Filippenko et al. 1992; Leibundgut et al. 1993; Turatto et al. 1996), SN 1999by (Garnavich et al. 2004), the transitional/91bg-like SN 2012ij (Li et al. 2022), and SN 1986G (Phillips et al. 1987). SN 2022xkq has a strong Ti II feature at maximum light, indicating a lower photospheric temperature than found in typical SNe Ia (Mazzali et al. 1997). This Ti II feature is similar to those seen in the spectra of the 91bg-like SNe, confirming the classification of SN 2022xkq. At peak SN 2022xkq is most spectroscopically analogous to SN 1986G, a highly reddened SN that is spectroscopically 91bg-like but has photometric properties not typical of 91bg-like SNe (for more in-depth discussion see Section 4).

The Si II $\lambda\lambda$5972 and 6355 absorption features are ubiquitous in SNe Ia. In SN 2022xkq, both of these Si II lines are asymmetric starting ∼10 days before peak and persisting to ∼3 days post-peak, though Si II λ6355 remains asymmetric until its disappearance. The Si II lines over these epochs are not well fit with a single Gaussian. When the Si II lines at −10 days relative to $B_{\max}$ are fit using a two-component Gaussian, we find a $13{,}000 \pm 500$ km s^{-1} component and a $10{,}000 \pm 500$ km s^{-1} component. We note that this is a small difference (∼3000 km s^{-1}) and that it is therefore difficult to determine whether there are truly two separate features (Silverman et al. 2015). 91bg-like SNe often exhibit asymmetric Si II absorption features (see Figure 7), possibly the result of a spectral-forming region located at higher velocities than for normal SNe Ia (Blondin et al. 2018) or of the blending of Fe II and Si II lines (Galbany et al. 2019). So while the observed asymmetry could indicate the presence of two velocity components, we refrain from making a definitive statement. We instead measure the velocities and EWs of Si II lines by fitting both with a fourth-degree spline. Using the location of the absorption trough, we find a Si II velocity of $11{,}920 \pm 350$ km s^{-1} in an early spectrum (−11.6 days) and 9980 ± 200 km s^{-1} near $B_{\max}$ (1.2 days). Near *B*-band maximum (1.2 days), we measure an EW of 38 ± 1 Å and 129 ± 7 Å for Si II $\lambda\lambda$5972 and 6355, respectively. These results are tabulated in Table 1.

SN 2022xkq's Si II velocities and EWs at $B_{\max}$ are similar to SN 1986G and close to other 91bg-like SNe. Polin et al. (2019) introduced the use of a plot of Si II λ6355 velocity and peak absolute *B*-band magnitude to identify SNe Ia that may be the result of sub-Chandrasekhar mass double-detonation explosions. Burrow et al. (2020) identify three subgroups of SNe Ia in this plot: "main," which may result from near-Chandrasekhar mass progenitors, and "fast" and "dim," both of which may have sub-Chandrasekhar mass progenitors with thin He shells (Polin et al. 2019). As shown in Figure 12, SN 2022xkq is a

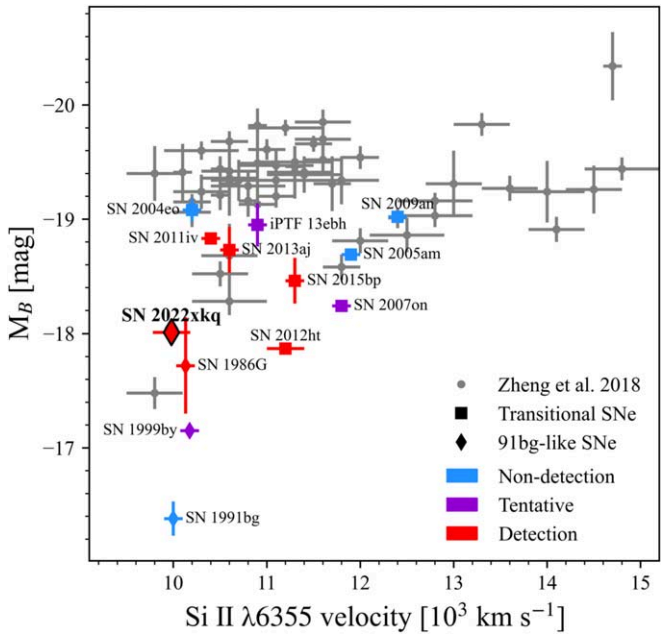

Figure 12. Plot of the *B*-band peak absolute magnitude vs. the Si II λ6355 velocity at B_{max} of SN 2022xkq compared to SNe Ia reported in Zheng et al. (2018), the transitional SN Ia sample (squares) presented in Wyatt et al. (2021, see their Table 7), and a few 91bg-like SNe Ia (stars): SN 1986G, SN 1991bg, and SN 1999by. Transitional and 91bg-like SN Ia points are colored based on whether C II λ6580 is observed in their early data. A tentative detection is illustrated by a "flat" profile in the C II region. C II classifications are taken from Wyatt et al. (2021) for transitional objects and from Ashall et al. (2016) for SN 1986G. In addition to SN 2022xkq, we classify SN 1991bg and SN 1999by.

dim SNe, consistent with other underluminous SNe Ia. We note that the frequency of C II λ6580 detection in dim SNe has raised questions about the mass of their progenitors (see Sections 6.3 and 8.2.1). The EWs of SN 2022xkq's Si II lines at peak are also similar to other 91bg-like SNe, which categorizes SN 2022xkq as "cool" in the Branch classification scheme (Branch et al. 2006; Burrow et al. 2020). Further, the Si II velocities of SN 2022xkq following explosion and at peak are consistent with other 91bg-like SNe (Wang et al. 2009). We note that Wang et al. (2009) exclude 91bg-like SNe from the normal-velocity (NV) and high-velocity (HV) classification scheme but that they roughly coincide with NV SNe.

6.2. Infrared Spectra

In addition to optical spectra, we also collected an infrared spectral sequence (see Figure 5). The pre-maximum light NIR evolution of SN 2022xkq is very similar to that of both SN 1999by and iPTF 13ebh. However, post-maximum light the NIR evolution is much closer to that of iPTF 13ebh than SN 1999by, which has more distinct absorption features in the *J* band than either SN 2022xkq or iPTF 13ebh.

There is a NIR feature around 2 μm that appears, both in emission and in absorption, in some of the NIR spectra. Given the lack of consistent evolution and the proximity of the nearby telluric region, we do not consider this feature real and do not mention it further.

Prominent iron-peak emission in the *H* band begins to appear around 5 days post-B_{max}. The blue-edge velocity, v_{edge}, of this feature can indicate the outer location of the Ni distribution. Assuming that the iron-peak emission begins at 1.57 μm (value used in Ashall et al. 2019), we measure v_{edge} of ∼11,000 km s^{-1} at 10 days post-B_{max} and ∼5500 km s^{-1} at 21 days post-B_{max}. This is in line with transitional SNe Ia like SN 2012ij (Li et al. 2022), SN 2015bp, and iPTF 13ebh (Ashall et al. 2019) but is significantly larger than 91bg-like SN Ia SN 1999by (Ashall et al. 2019). This behavior may indicate a Ni distribution similar to that of transitional SNe Ia, though we note that SN 1999by is the only other 91bg-like SN Ia for which robust NIR observations exist.

6.3. Optical and Infrared Carbon Detection

The presence of C lines in the early spectra can provide important constraints on the explosion mechanisms of SNe Ia. SN 2022xkq displays both optical C II λ6580 and NIR C I λ10693 in the pre-B_{max} spectra (see Figure 13). We compare the evolution of the carbon features in SN 2022xkq to that of other transitional/91bg-like SNe Ia that also exhibit strong carbon features: SN 1999by, iPTF 13ebh, and SN 2015bp.

The optical carbon absorption feature in SN 2022xkq is clear in the earliest spectra before weakening to a "flat" feature by −7 days post-B_{max} and disappearing soon after. This evolution, though more rapid, is similar to what was observed in SN 2015bp (Wyatt et al. 2021). In contrast, iPTF 13ebh, despite its strong NIR carbon feature, has a flat C II λ6580 profile in the earliest epochs that quickly fades. The optical carbon observed in SN 1999by also has a flat C II pre-maximum, though this feature persists much closer to peak than observed in SN 2022xkq.

Based on the classification scheme of Folatelli et al. (2012), the clear presence of C II λ6580 in the spectra from −13 to −9 days of SN 2022xkq can be classified as "A" (i.e., absorption), for a clear C II λ6580 feature in the earliest spectrum. This is also the classification assigned to SN 2015bp. In contrast, iPTF 13ebh was classified as "F," named for the flat profile on the red side of Si II λ6355, which indicates a marginal detection of C II λ6580. SN 1999by was also classified as F, though its earliest optical spectrum is from a significantly later epoch (−3 days relative to the time of B_{max}) than SN 2022xkq or iPTF 13ebh, which prevents the detection of an earlier, and perhaps stronger, carbon feature. No C II λ6580 (classified as "N") was observed in SN 1991bg, though the lack of early spectra likely precludes its detection. Most transitional/91bg-like SNe with early optical spectra show evidence for the presence of C II λ6580 in some capacity (see Figure 12), including SN 2022xkq. We note that this feature has been attributed to Fe II λ6516 in some of the 91bg-like SNe (Galbany et al. 2019); however, we do not observe any strong Fe II lines (i.e., λλ6456, 6516, 7308, 7462, 7711) within this wavelength region in SN 2022xkq.

The earliest NIR spectrum of SN 2022xkq was taken only 3 days after the initial detection of the SN. This spectrum, as well as several subsequent spectra, exhibits a feature at 1.03 μm on the blue side of the Mg II 1.09 μm multiplet. This feature is analogous to those observed in the early NIR spectra of several other transitional/91bg-like SNe (e.g., SN 1999by, iPTF 13ebh, and SN 2015bp), where it was identified as C I λ10693. Further, as shown in Figure 13, this feature has a similar velocity evolution to C II λ6580. We therefore identify this line as C I λ10693. We note that this feature has also been suggested to be He I λ10830 (Boyle et al. 2017; Collins et al. 2023), and we explore this possibility in Section 8.2.3.

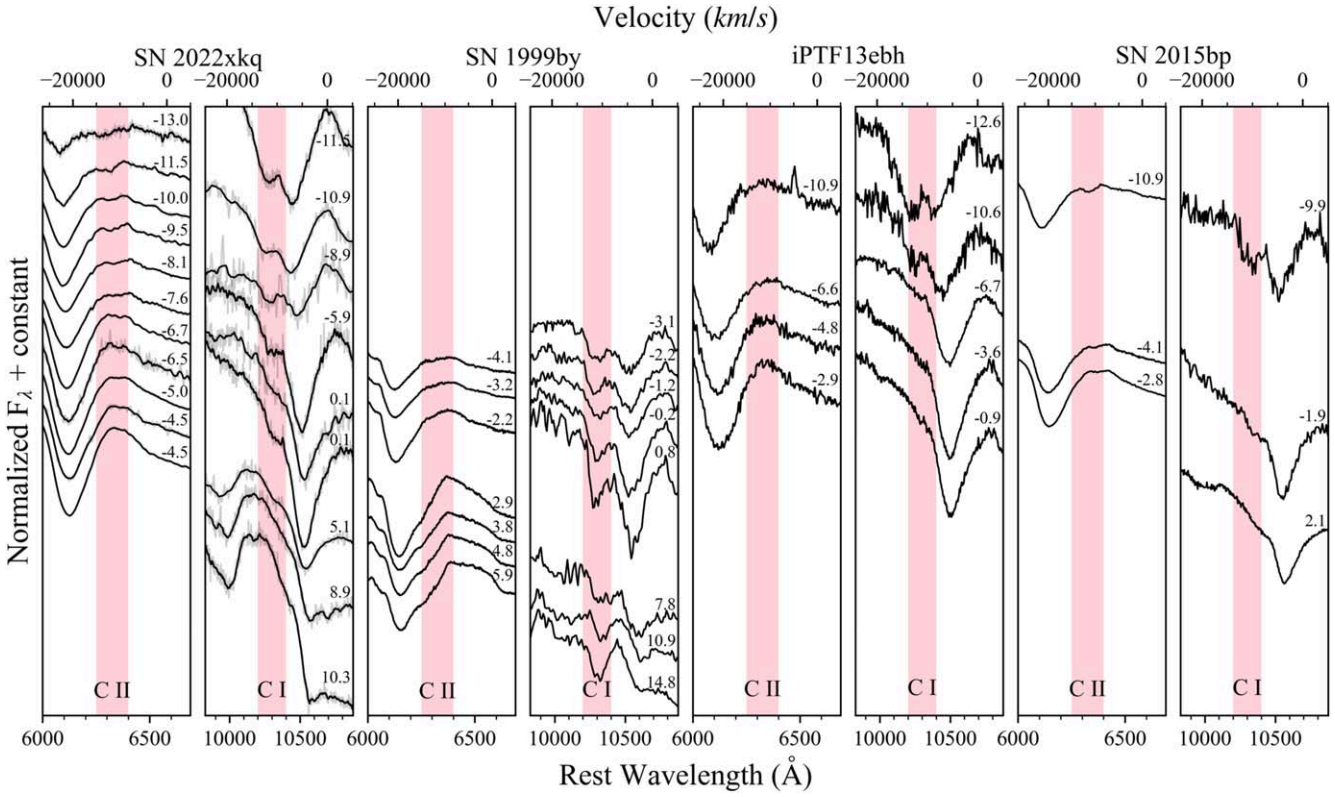

Figure 13. The optical C II λ6580 and NIR C I λ10693 evolution of SN 2022xkq compared to transitional/91bg-like SNe Ia: SN 1999by (Höflich et al. 2002; Garnavich et al. 2004), SN 2015bp (Wyatt et al. 2021), and iPTF 13ebh (Hsiao et al. 2015). The C II evolution of SN 2022xkq is similar to that of SN 2015bp, starting with a strong C II line that evolves to a "flat" feature before disappearing near $B_{\rm max}$. SN 2022xkq also has a strong NIR C I λ10693 feature that persists until ∼5 days post-$B_{\rm max}$, which is somewhat comparable to the NIR C I evolution in SN 1999by.

The line we identify as C I λ10693 persists past $B_{\rm max}$ and is still present at +5 days with respect to B-band maximum (see Figure 13). In the earliest spectra, SN 2022xkq has a C I λ10693 feature similar in shape to that of iPTF 13ebh (Hsiao et al. 2015), which displays a strong feature in the −13- and −11-day spectra, but the feature has weakened significantly by −7 days. The persistence of the C I λ10693 feature in SN 2022xkq is most analogous to that of SN 1999by, which displays a strong C I λ10693 feature post-$B_{\rm max}$ as well. However, the C I λ10693 feature in SN 1999by is still present at 15 days post-$B_{\rm max}$. Höflich et al. (2002) suggested that there may have also been a strong C I λ9406 feature in SN 1999by given the strength of the C I λ10693 line. However, we do not detect C I λ9406 in the spectra of SN 2022xkq. The C I λ10693 in SN 1999by persists for much longer than observed in SN 2022xkq, where the feature has mostly disappeared after 5 days post-$B_{\rm max}$. We note that in the 9- and 10-day NIR spectra of SN 2022xkq there is a shoulder in the Mg II λ10927 feature; this shoulder has been linked to fading C I λ10693 (Hsiao et al. 2015), so the NIR carbon may be present even past 5 days after the time of $B_{\rm max}$.

SN 2022xkq exhibits more persistent carbon lines, in both the optical and NIR, than those observed in either iPTF 13ebh or SN 2015bp. Of the three transitional/91bg-like SNe Ia with clear NIR carbon features to which we compare, perhaps only SN 1999by displays evidence of stronger carbon than observed in SN 2022xkq. With the addition of SN 2022xkq, the sample of transitional/91bg-like SNe Ia with carbon features indicates that these lines may be commonplace in underluminous SNe. This is perhaps not a surprising result, as several authors (Thomas et al. 2011; Maguire et al. 2014) have noted a correlation between narrow light curves, denoted by low s_{BV} values, and the presence of carbon. The detection of carbon in SN 2022xkq may have significant implications for the explosion mechanism of the SN; this is further discussed in Section 8.2.

6.4. H and He Constraints from Nebular Spectroscopy

To place further constraints on the progenitor of SN 2022xkq, we use the late-time, low-resolution ($R \approx 650$), high signal-to-noise ratio spectrum taken using the LDSS-3 spectrograph at the Magellan Clay telescope +118 days post-$B_{\rm max}$. If the progenitor system of SN 2022xkq has a nondegenerate companion, models indicate that the SN ejecta will ablate part of its envelope, resulting in narrow hydrogen or helium emission lines $\gtrsim$100 days after explosion (most recently Boehner et al. 2017; Botyánszki et al. 2018; Dessart et al. 2020). Models predict $\gtrsim$0.1 $M_\odot$ of stripped hydrogen (Botyánszki et al. 2018; Dessart et al. 2020); however, there is diversity in the predicted shape and strength of the Hα emission line based on the details of the SN explosion, the companion, and treatment of non-LTE effects.

There are no hydrogen or helium emission features visible in the LDSS-3 spectrum (see Figure 4). Using the methodology of Sand et al. (2018, 2019, 2021), we set limits on narrow Hα and He I ($\lambda\lambda$5875, 6678) emission. We note that the NIR spectrum taken at +103 days has too low signal-to-noise ratio to perform a meaningful analysis on the He I λ10830 line. The extinction-corrected and flux-calibrated spectrum is binned to the native resolution and smoothed on scales larger than the expected

emission (FWHM $\approx$ 1000 km s^{-1}) using a second-order Savitzky & Golay (1964) filter with a width of 132 Å. Hydrogen and helium emission features with widths similar to those expected from a single-degenerate scenario would be apparent when comparing the unsmoothed and smoothed versions of the spectrum.

We insert emission lines with width 1000 km s^{-1} and a peak flux five times the rms of the residual spectrum into our data in order to set quantitative limits on the Hα and He I nondetections. As shown in Table 1, the resulting flux and luminosity limits (assuming $D = 31$ Mpc) are (1) Hα of 7.6×10^{-17} erg s^{-1} cm^{-2} and 8.8×10^{36} erg s^{-1}, (2) He I λ5875 of 3.4×10^{-16} erg s^{-1} cm^{-2} and 4.0×10^{37} erg s^{-1}, and (3) He I λ6678 of 7.6×10^{-17} erg s^{-1} cm^{-2} and 8.8×10^{36} erg s^{-1}. For reference, the Hα luminosity limit for SN 2022xkq is between $\sim$4 and 10 times fainter than the Hα detections seen in three recent low-luminosity, fast-declining SNe Ia with similar photometric properties to SN 2022xkq (Kollmeier et al. 2019; Vallely et al. 2019; Prieto et al. 2020; Elias-Rosa et al. 2021), indicating that we would detect such features if they were present.

First, we use the radiation transport model sets from Botyánszki et al. (2018) to translate the hydrogen and helium luminosity limits to masses. The 3D radiation transport results of Botyánszki et al. (2018) present simulated SN Ia spectra 200 days after explosion based on the ejecta–companion interaction simulations of Boehner et al. (2017); see Botyánszki et al. (2018) for further details. The simulated spectra presented in Botyánszki et al. (2018) have $L_{\mathrm{H}\alpha} \approx (4.5\text{–}15.7) \times 10^{39}$ erg s^{-1} ($M_{\mathrm{strip}} \sim 0.2\text{–}0.4\ M_{\odot}$) for the main-sequence, subgiant, and red giant companion star models. This is roughly 500–1800 times brighter than the detection limit for SN 2022xkq. In order to quantify the stripped mass limit for SN 2022xkq, we adopt the quadratic fitting relation between Hα (and He I $\lambda\lambda$5875 and 6678) luminosity and stripped hydrogen (/helium) mass (Equation (1) in Botyánszki et al. 2018 as updated by Sand et al. 2018) and correct for the epoch of our observations (118 days after B_{max} or 133 days after explosion; see Botyánszki et al. 2018). This yields a stripped hydrogen mass limit of $M_{\mathrm{H,strip}} \lesssim 2 \times 10^{-4} M_{\odot}$ and a helium mass limit of $M_{\mathrm{He,strip}} \lesssim 2 \times 10^{-3} M_{\odot}$ and $M_{\mathrm{He,strip}} \lesssim 7 \times 10^{-4} M_{\odot}$ for the He I $\lambda\lambda$5875 and 6678 lines, respectively.

We also constrain the amount of stripped hydrogen based on 1D non-LTE radiative transfer calculations of several delayed-detonation models (Blondin et al. 2013; DDC0, DDC15, and DDC25) presented in Dessart et al. (2020). We interpolate the available model grid, 100–300 days post-explosion, to the explosion epoch of SN 2022xkq. This gives a stripped hydrogen mass of $M_{\mathrm{H,strip}} \lesssim 7 \times 10^{-5}\ M_{\odot}$ with very little variation between the models. Dessart et al. (2020) do not present a luminosity-to-mass conversion for helium, so we do not derive a stripped helium mass for this model.

Limits on hydrogen and helium luminosity and stripped mass are listed in Table 1. Other narrow emission lines, such as [O I] λ6300 and Ca II $\lambda\lambda$7291 and 7324, may be sensitive to helium star companions in particular (e.g., Lundqvist et al. 2013). The LDSS-3 spectrum of SN 2022xkq constrains the luminosity of [O I] λ6300 to be $L_{[\mathrm{O\,I}]} < 8.8 \times 10^{36}$ erg s^{-1}. Further collection of nebular spectra of SN 2022xkq is needed to search for signatures of a single-degenerate scenario at later times. This is especially important given the detection of Hα in several similar low-luminosity SNe Ia (Kollmeier et al. 2019; Vallely et al. 2019; Prieto et al. 2020; Elias-Rosa et al. 2021).

7. Radio Nondetection

We have modeled any possible radio emission from SN 2022xkq in the same way as in Lundqvist et al. (2020) and Hosseinzadeh et al. (2022b)—that is, we assume that any emission would arise as a result of circumstellar interaction. Behind the SN blast wave, electrons are accelerated to relativistic speeds, magnetic fields are generated, and the relativistic electrons thereby radiate synchrotron emission. For a power-law distribution of the electron energies, $dN/dE = N_0 E^{-p}$, where $E = \gamma m_e c^2$ is the energy of the electrons and γ is the Lorentz factor, the intensity of optically thin synchrotron emission $\propto \nu^{-\alpha}$, where $\alpha = (p-1)/2$. We have adopted $p = 3$ (Chevalier & Fransson 2006). The structure of the circumstellar medium depends on the progenitor system. For a double-degenerate progenitor system, a constant density medium may be expected (as might be expected for relatively undisturbed interstellar medium), whereas for the single-degenerate scenario we might expect the circumstellar environment to be shaped by the companion star and binary processes. In this case, we assume wind-like circumstellar medium described by a constant mass-loss rate ($\dot{M}$) and a constant wind speed (v_w), implying a density decrease with radius as $\rho(r) = \dot{M}/(4\pi r^2 v_w)$. We assume a constant function of post-shock energy density from amplified magnetic fields, defined as $\epsilon_B = u_B/u_{\mathrm{th}}$, where u_{th} is the post-shock thermal energy density ($\sim \rho v_s^2$, where v_s is the velocity of the shock) and u_B is the magnetic field energy density. We use the model N100 (Röpke et al. 2012; Seitenzahl et al. 2013) for the SN ejecta to test the single-degenerate scenario. To the fastest ejecta in the model ($\sim 2.8 \times 10^4$ km s^{-1}) we add even faster ejecta with a density profile $\rho_{ej} \propto r^{-n}$ with $n = 13$ (see Kundu et al. 2017, for a discussion on n). In both models, we also assume a constant function of post-shock energy density from relativistic electrons, $\epsilon_{\mathrm{rel}} = 0.1$, where $\epsilon_{\mathrm{rel}} = u_{\mathrm{rel}}/u_{\mathrm{th}}$, and u_{rel} is the energy density in relativistic electrons. For the brightness temperature of the radio emission at the frequency at which the optical depth of synchrotron self-absorption is unity we adopt $T_{\mathrm{bright}} = 5 \times 10^{10}$ K (see Björnsson & Lundqvist 2014, for a discussion on T_{bright}).

In Figure 14 we show the predicted radio emission from our wind model. We have assumed that the explosion occurs 3.5 days prior to the epoch of radio data, i.e., 1 day before detection in the optical. The ratio of $\dot{M}/v_w$ has been tuned to give the highest luminosity possible that does not conflict with the observational radio limits. Solid (dashed) lines are for $\epsilon_B = 0.1$ (0.01). A higher wind density is needed to compensate for less efficient conversion to magnetic field energy density, and we obtain $\dot{M} \lesssim 2.1\ (11.0) \times 10^{-8}\ M_{\odot}\ \mathrm{yr}^{-1}\ (v_w/100\ \mathrm{km\ s}^{-1})$ for $\epsilon_B = 0.1$ (0.01). The observed upper limit at 9.0 GHz constrains the models the most, and for the $\epsilon_B = 0.1$ (0.01) model the circumstellar shock is at $\approx 2.4\ (1.9) \times 10^{15}$ cm 3.5 days after explosion. The figure also shows a model with $\dot{M} = 9.3 \times 10^{-6}\ M_{\odot}\ \mathrm{yr}^{-1}\ (v_w/100\ \mathrm{km\ s}^{-1})$ and $\epsilon_{\mathrm{rel}} = 0.1$ (dotted lines). For higher wind densities than this, synchrotron self-absorption becomes so large that the modeled emission is predicted to fall below the observed luminosity at 9.0 GHz. So, in essence, our models can only rule out the interval $\dot{M} = (2.1 \times 10^{-8}$ to $9.3 \times 10^{-6}) M_{\odot}\ \mathrm{yr}^{-1}\ (v_w/100\ \mathrm{km\ s}^{-1})$ for $\epsilon_B = 0.1$. However, since multiepoch radio observations have limited $\dot{M}$ to a few $\times 10^{-8} M_{\odot}\ \mathrm{yr}^{-1}\ (v_w/100\ \mathrm{km\ s}^{-1})$ for many SNe Ia (Chomiuk et al. 2016; Lundqvist et al. 2020), with the notable exception of SN Ia–CSM (Kool et al. 2023), the $\dot{M}$ value

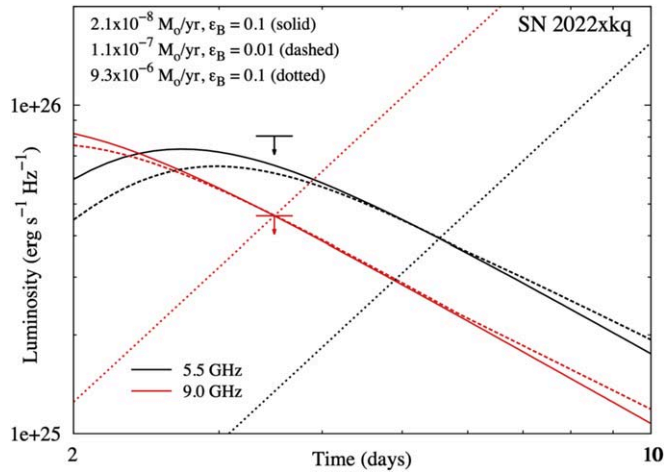

Figure 14. Radio data for SN 2022xkq (Ryder et al. 2022), together with models at 5.5 GHz and 9.0 GHz for a $\rho(r) \propto r^{-2}$ wind. Models use $\dot{M} = 2.1\,(11.0) \times 10^{-8} M_\odot\ \mathrm{yr}^{-1}\ (v_w/100\ \mathrm{km\ s}^{-1})$ for $\epsilon_B = 0.1\,(0.01)$, with solid (dashed) lines being for $\epsilon_B = 0.1\,(0.01)$. Common parameters in both models are $\epsilon_e = 0.1$, $T_{\mathrm{bright}} = 5 \times 10^{10}$ K, $n = 13$, and $v_w = 100$ km s^{-1}. The most constraining observation is that at 9.0 GHz on day 3.5. As there is only one epoch of observations, there is also an upper limit on the derived mass-loss rate shown here for $\epsilon_B = 0.1$ as dotted lines. See text for more details.

highlighted by the dotted lines in Figure 14 should only be considered as a formal limit.

To test the double-degenerate scenario, we have used a constant density for the ambient medium. In this case the modeled radio flux increases with time (e.g., Chomiuk et al. 2012, 2016; Kundu et al. 2017; Lundqvist et al. 2020). The progenitor model used is the violent merger model by Pakmor et al. (2012), simulating the merger of two C/O degenerate stars with masses 1.1 and $0.9\,M_\odot$. The total mass and asymptotic kinetic energy of the ejecta for this model are $1.95\,M_\odot$ and 1.7×10^{51} erg, respectively. We assume the same $n = 13$ density profile for this model as for the single-degenerate model. Again, the 9.0 GHz data are the most constraining, and we obtain an upper limit on the density of the ambient medium of 1450 (9800) cm^{-3} for $\epsilon_B = 0.1\,(0.01)$. For the $\epsilon_B = 0.1\,(0.01)$ model the circumstellar shock is at $\approx 2.6\,(2.1) \times 10^{15}$ cm 3.5 days after explosion.

In summary, the radio data can be used to put a limit on the density of the ambient medium outside $\sim 2 \times 10^{15}$ cm. In a single-degenerate scenario, the mass-loss rate of the progenitor system is $\lesssim 2.1 \times 10^{-8}\,M_\odot\ \mathrm{yr}^{-1}\ (v_w/100\ \mathrm{km\ s}^{-1})$ for $\epsilon_B = 0.1$. When we compare these limits to the mass-loss rate parameters of single-degenerate models defined by Chomiuk et al. (2012), we find that these limits are deep enough to rule out most symbiotic systems (red giant companions). These systems are characterized by slow winds (10–100 km s^{-1}) and mass-loss rates of 10^{-6} to $10^{-8}\,M_\odot\ \mathrm{yr}^{-1}$ (Seaquist & Taylor 1990). Radio upper limits have ruled out red-giant companions for the majority of SNe Ia (Chomiuk et al. 2012; Horesh et al. 2012; Pérez-Torres et al. 2014; Chomiuk et al. 2016; Lundqvist et al. 2020; Pellegrino et al. 2020; Burke et al. 2021; Hosseinzadeh et al. 2022b, 2023b). However, many models involving main-sequence companions still lie within the radio limits for SN 2022xkq. For the double-degenerate scenario, or the single-degenerate scenario with spun-up/spun-down super-Chandrasekhar-mass white dwarfs (Di Stefano et al. 2011; Justham 2011), where mass transfer no longer occurs at the time of explosion, a near-uniform density of the ambient medium is expected. However, the early radio data here are not ideal to test this since the likely number density is of order 1 cm^{-3}, and our upper limit on the density is 1450 cm^{-3} for $\epsilon_B = 0.1$. The limits on mass-loss rates and ambient medium density are a factor of ≈5–7 larger for $\epsilon_B = 0.01$. Given that the radio flux is expected to increase with time in the case of interaction with uniform medium (Chomiuk et al. 2016), we encourage further monitoring of this SN in order to obtain more stringent limits.

8. Discussion

8.1. Origin of the Red Excess

Several SNe Ia exhibit early flux excesses in the UV and bluer optical bands (Hosseinzadeh et al. 2017; Miller et al. 2020a; Burke et al. 2021; Hosseinzadeh et al. 2022b, 2023b; Srivastav et al. 2023; Wang et al. 2023). Population studies of SNe Ia have suggested that these "blue bumps" may be a common occurrence (Burke et al. 2022a, 2022b; Deckers et al. 2022; Magee et al. 2022). However, red flux excesses are much less common. Only a handful of SNe Ia have been suggested to have an early time "red excess," notably MUSSES1604D (Jiang et al. 2017), SN 2018aoz (Ni et al. 2022), and the more peculiar SN 2018byg (De et al. 2019) and SN 2022joj (Padilla Gonzalez et al. 2023; Liu et al. 2023). Ni et al. (2023b) suggest that SN 2021aefx may also have had a red flux excess, although it was not characterized this way by other authors (Hosseinzadeh et al. 2022b; Ashall et al. 2022).

Jiang et al. (2017) attribute the red excess in MUSSES1604D to double detonation, where the He-shell detonation produces radioactive isotopes in the outer ejecta layers, creating an early flux excess. The He-shell detonation also creates iron-group and intermediate-mass elements, like Ti and Ca, which primarily absorb in the blue optical bands, thus blocking the blue flux and producing an overall red $B - V$ color. The early bump in the light curve of MUSSES1604D was thus attributed to a flash produced by decaying radioactive isotopes. Ni et al. (2023a) give three possible explanations for the red flux excess in SN 2018aoz: (1) surface radioactive isotopes, (2) interaction with a binary companion, and (3) interaction with surrounding circumstellar material. They note that, similar to MUSSES1604D, some Fe-group line blanketing is required to produce the observed color evolution; therefore, any scenario will likely include the production of radioactive materials in the outer ejecta. Similarly, the red excesses in SN 2018byg and SN 2022joj have also been linked to double detonation and iron-group element absorption in the blue. However, double-detonation models cannot reproduce the observed C II features in SN 2022joj (Padilla Gonzalez et al. 2023; Liu et al. 2023). For SN 2021aefx, double detonation has been used to explain the UV suppression and the early redder color (Ni et al. 2023b). However, Hosseinzadeh et al. (2022b) note that there are observational features of SN 2021aefx that do not support a double-detonation scenario, including the presence of carbon lines at pre-maximum epochs and the lack of strong [Ca II] emission in the nebular spectra.

Other origins for an early red color in SNe Ia have also been suggested. ZTF 18aayjvve and ZTF 18abdfwur were identified as possibly having red excesses, but neither were well explained by a double-detonation scenario and were better explained as the result of the presence of ^{56}Ni in the outer layers or companion/CSM interaction (Deckers et al. 2022).

As we discuss further below, we do not favor a double-detonation mechanism for SN 2022xkq, but we cannot rule it out. A wide variety of explosion parameters can significantly change the color evolution of double-detonation explosions, including the exact mass of the white dwarf progenitor and the He shell (Kromer et al. 2010; Shen et al. 2010; Sim et al. 2012; Polin et al. 2019), the degree of mixing (Polin et al. 2019; Gronow et al. 2020), non-LTE effects (Shen et al. 2021a; Dong et al. 2022), and viewing angle effects (Kromer et al. 2010; Sim et al. 2012; Gronow et al. 2020; Shen et al. 2021b). Viewing angle effects in particular have been shown to have a significant impact on the color, light-curve morphology, and spectral evolution of double-detonation SNe (Sim et al. 2012; Gronow et al. 2020; Shen et al. 2021b). We also cannot discount impacts from other processes that might result in bluer early colors in more luminous SNe Ia, like companion and CSM interaction. The strong Ti absorption features that denote 91bg-like SNe dominate in U and B bands and may suppress any blue bumps, resulting in a red early color. Further modeling is needed to understand the origin of the early red color excess in SN 2022xkq.

8.2. Further Explosion Constraints

The progenitors and explosion mechanisms of transitional/91bg-like SNe Ia are the subject of some debate. Studies have long suggested double detonation in sub-Chandrasekhar mass white dwarfs as the origin for faint SNe Ia (Goldstein & Kasen 2018; Polin et al. 2019; Shen et al. 2021b; Collins et al. 2023). However, the analyses of a few transitional and 91bg-like SNe suggest that many of these objects are best described by the delayed detonation of near-Chandrasekhar mass white dwarfs (Höflich et al. 2002; Ashall et al. 2016, 2018). One of the differentiators between these two scenarios is the amount of unburnt carbon in the ejecta. Here we discuss the presence of carbon in sub-Chandrasekhar mass models, both pure and double detonation, and compare the spectra of SN 2022xkq with models of a Chandrasekhar mass delayed detonation and pure sub-Chandrasekhar mass detonation to try to shed further light on the origins of this SN. Finally, it has been suggested that the double-detonation scenario may produce a He I line that could be misidentified as C I (Boyle et al. 2017; Collins et al. 2023); we discuss this possibility in Section 8.2.3.

8.2.1. Carbon in Sub-Chandrasekhar Mass Models

The carbon lines observed in SN 2022xkq, as well as other transitional/91bg-like SNe Ia, can be difficult to reconcile with sub-Chandrasekhar mass progenitors. For underluminous SNe Ia both pure and double-detonation sub-Chandrasekhar mass models have higher carbon-burning efficiencies, resulting in less unburnt carbon than Chandrasekhar mass models with similar ^{56}Ni masses and therefore weaker or nonexistent carbon features. However, we note that the actual amount of unburnt carbon is model dependent.

In the double-detonation sub-Chandrasekhar models presented by Polin et al. (2019), the amount of unburnt carbon left following detonation would not produce optical carbon features in the spectra of an SN Ia. However, the sub-Chandrasekhar mass models presented in Blondin et al. (2017) have NIR carbon in the spectra pre-maximum light. We note that the Blondin et al. (2017) models are of pure central detonation of a bare CO white dwarf and do not account for any He-shell effects that could potentially result in less unburnt carbon. Neither Polin et al. (2019) nor Blondin et al. (2017) predict the presence of optical carbon in the spectra of an SN Ia produced by a sub-Chandrasekhar mass progenitor. The Blondin et al. (2017) models produce a feature on the red wing of Si II λ6355, though this feature is due to the Mg II λ6347 doublet rather than C II λ6580. Given that the amount of unburnt carbon following the detonation (whether pure or double) of a sub-Chandrasekhar white dwarf is dependent on the physical parameters of the model, we caution against using the presence of carbon as the sole indicator of the progenitor.

8.2.2. Sub-Chandrasekhar versus Delayed Detonation

Blondin et al. (2017) modeled the explosion of a transitional SN Ia using two types of explosion models: Chandrasekhar mass delayed-detonation models with nickel masses of 0.3 and 0.21 $M_{\odot}$, denoted as DDC20 and DDC22, respectively; and models of the pure central detonation of a sub-Chandrasekhar 0.95 and 0.93 $M_{\odot}$ white dwarf (^{56}Ni masses of 0.23 and 0.17 $M_{\odot}$) labeled as SCH3p0 and SCH2p5, respectively. We compare these four models to the spectra of SN 2022xkq in Figure 15. For the optical spectra (left panel), we scale all models to the wavelength weighted average flux from 6000 to 7500 Å of the comparison spectra of the same epoch; this region was chosen because it is primarily continuum absorption. In the NIR (right panel), models were similarly scaled to the spectral region from 10,000 to 13,000 Å, a region with little influence from telluric lines.

We find that immediately following explosion (<-7 days from time of $B_{\rm max}$) the pure sub-Chandrasekhar mass models are a somewhat better reproduction of the shape of the optical spectra of SN 2022xkq compared to the delayed-detonation models; this is most evident on the blue end of the optical spectra (see Figure 15, left panel). We note, however, that the pure sub-Chandrasekhar mass models are still too red to map the 4000–6000 Å region at early times. A week before $B_{\rm max}$ and beyond, of the sub-Chandrasekhar mass models SCH3p0 is a slightly better representation, though at peak SCH2p5 matches the optical data remarkably well. Despite being not blue enough at early times, the DDC20 delayed-detonation explosion also matches the observations near and after peak light.

In the infrared, the pure-detonation sub-Chandrasekhar mass models have features with higher velocities than observed in SN 2022xkq at early times. At peak light, the sub-Chandrasekhar mass models are a slightly better match to the data than the delayed-detonation models. However, in the early spectra the delayed-detonation models reproduce the NIR C I feature better than the pure-detonation sub-Chandrasekhar mass models. The pure sub-Chandrasekhar mass models have more C I λ10693 than the delayed-detonation models immediately following explosion since the line-forming region is located at higher velocities, where the carbon abundance is significantly higher. Conversely, neither the sub-Chandrasekhar mass nor the delayed-detonation Chandrasekhar mass models display C II λ6580 since its line formation region is located in the ejecta layers where the carbon abundance is too low. All of the models reproduce the evolution of the NIR C I line in the spectra, strongest immediately following explosion and then eventually weakening and disappearing. However, none of the models to which we compare have carbon post-maximum light.

Given the less pronounced Sc II/Ti II absorption trough around 4000–4200 Å and the decent match to the optical and

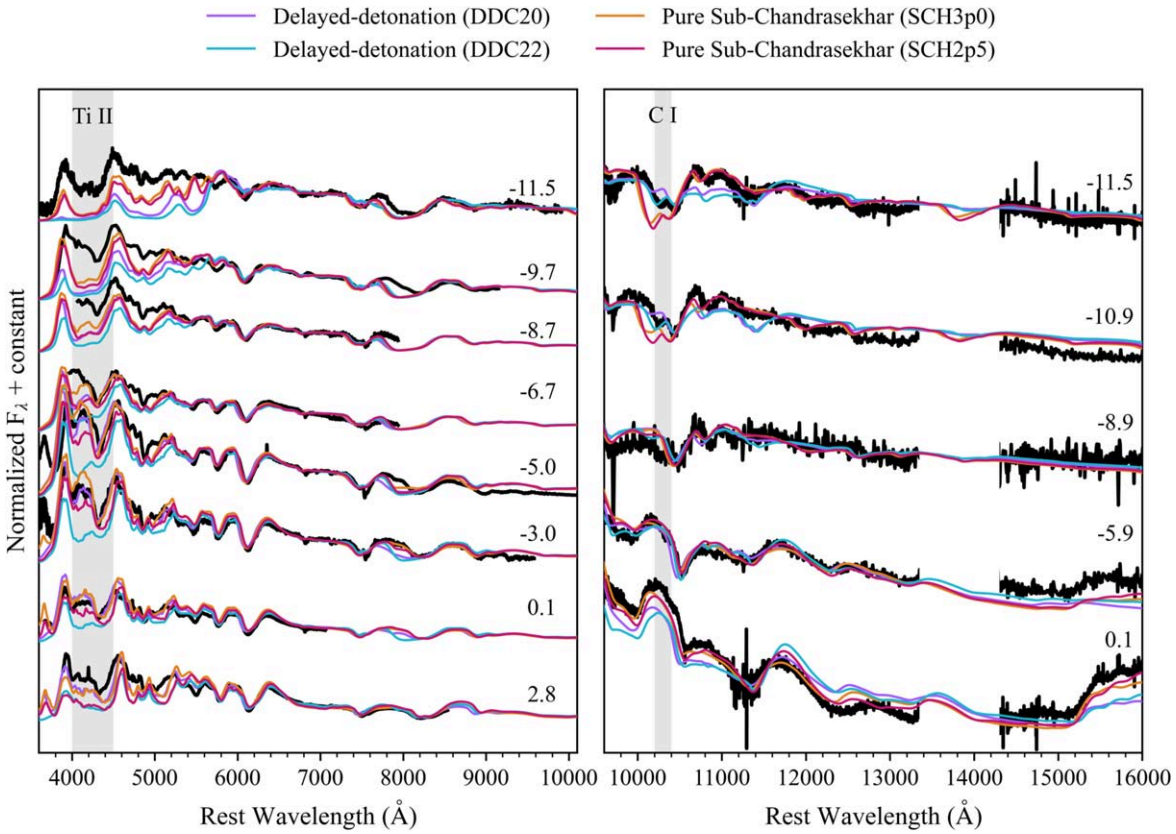

Figure 15. Optical and NIR spectra of SN 2022xkq compared to models of delayed-detonation and pure-detonation sub-Chandrasekhar mass explosions from Blondin et al. (2017). Optical models are scaled to the weighted average flux from 6000 to 7500 Å of the spectrum to which they are compared, and NIR models are scaled to the wavelength weighted average flux from 10,000 to 13,000 Å. The spectral evolution of SN 2022xkq is closer to the models of the pure detonation of a sub-Chandrasekhar mass white dwarf. Phases are relative to the time of B_{max}. The input models and synthetic spectra shown in this figure are publicly available on Zenodo (Blondin et al. 2023).

infrared spectral evolution near maximum light, the observations of SN 2022xkq are closer to the pure sub-Chandrasekhar mass white dwarf model. However, we note that pure central detonation is only an approximation and the detonation mechanism will have significant impacts on the spectral evolution. Further, modeling uncertainties in nucleosynthesis and burning front propagation can have significant impacts on carbon abundance in delayed-detonation models. Other delayed-detonation models have shown considerable promise in describing the general spectral evolution, including the C II λ6580 and NIR C I features, of other SNe similar to SN 2022xkq, including SN 1986G (Höflich et al. 2002; Ashall et al. 2016, 2018). Ultimately, neither of the models to which we compare was designed for SN 2022xkq, which has an inferred ^{56}Ni mass that falls between these models, and dedicated work may result in models that more closely follow the evolution of the SN for either scenario.

8.2.3. Helium in Double-detonation Models

In double-detonation models, the surface detonation of helium can result in observable trace amounts of unburnt helium in the outer ejecta of the SN. These helium features are difficult to model since their optical depth depends on the treatment of non-LTE effects, the evolution of the velocity gradient, the ejecta density, variations in radiation temperature, the viewing angle, and so on (Kromer et al. 2010; Boyle et al. 2017; Shen et al. 2021b; Collins et al. 2023). Boyle et al. (2017) present the expected evolution of NIR He I 1.0830 and 2.0581 μm in both "high-mass" (1.025 $M_\odot$ CO core mass) and "low-mass" (0.58 $M_\odot$ CO core mass) models. The high-mass model corresponds to normal-luminosity SNe Ia (Fink et al. 2010). The low-mass model is designed to describe underluminous, peculiar thermonuclear events (Sim et al. 2012). SN 2022xkq is an intermediate case, though closer in luminosity to the low-mass model. The helium absorption lines are much stronger in the low-mass model, where more helium remains in the ejecta. However, both low- and high-mass models have prominent He I 1.0830 μm features that somewhat resemble the absorption features we identify as C I 1.0693 μm in Figure 13.

In both the high- and low-mass models, helium is visible at maximum light and grows stronger past maximum (Boyle et al. 2017). In contrast, the observed feature in SN 2022xkq gets weaker post-maximum rather than stronger. However, Collins et al. (2023) recently presented a sub-Chandrasekhar mass double-detonation model in which helium is strongest immediately following explosion and fades near peak luminosity. This model plausibly reproduces the C I feature in iPTF 13ebh with just He I 1.0830 μm. Therefore, the evolution of the observed feature in SN 2022xkq could be explained by either helium or carbon.

The model presented in Collins et al. (2023) does reproduce the flat profile of C II λ6580 observed in iPTF 13ebh, so optical carbon features alone cannot be used to confirm the presence of NIR C I. Instead, we use other He I features to determine whether the C I 1.0693 μm feature is actually due to He I

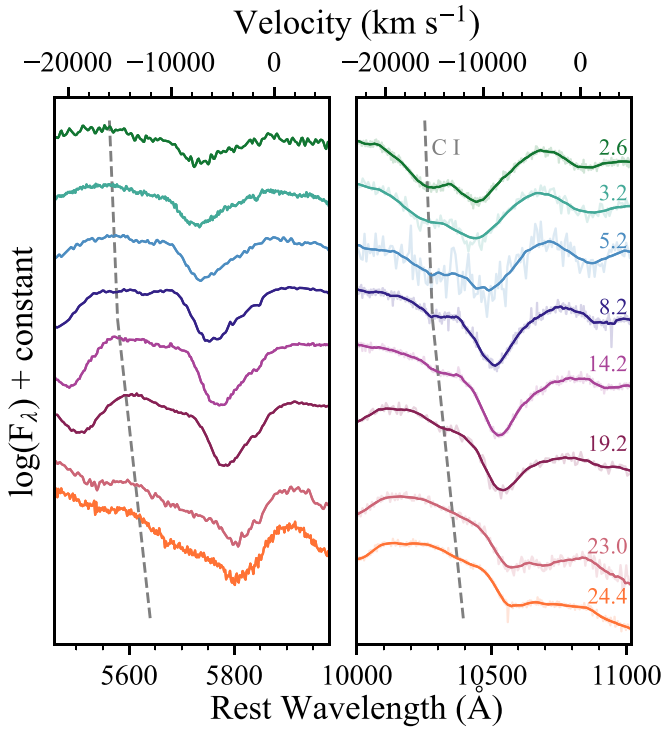

Figure 16. The evolution of the region where the He I $\lambda\lambda$5875 and 10830 lines are expected to appear in the infrared spectra. Labeled epochs are the time since explosion as determined by a power-law fit. The feature we identify as C I λ10693 is marked in the right panel with the dashed line. If this feature were He I λ10830 rather than C I, there would be a corresponding He I λ5875 feature in the earliest spectra (marked by the dashed line in the left panel). There is no notable absorption feature from He I λ5875, indicating that the feature on the blue wing of Mg II is likely C I λ10693 rather than He I λ10830.

1.0830 μm. We cannot properly assess whether there is a He I 2.0581 μm absorption feature given its proximity to the nearby telluric region. The next-strongest He I line in the Collins et al. (2023) models is He I λ5875. This line is blended with other lines in the region and is completely gone by ∼9 days after explosion but is detectable in earlier spectra. The earliest infrared spectrum of SN 2022xkq was taken just 2.6 days after explosion. This is well within the period in which we would expect to observe He I λ5875 given the strength of the potential He I 1.0830 μm line. As shown in Figure 16, there is no clear detection of He I λ5875 at the expected He I velocity. Therefore, there is no evidence that the NIR feature at 1.03 μm is He I 1.0830 μm.

Based on current models, we are unable to suggest either the delayed-detonation or the double-detonation scenario as the explosion mechanism of SN 2022xkq at this time. More tailored modeling would be needed to determine the origin of this SN.

9. Summary and Conclusions

SN 2022xkq is one of the best-observed underluminous SNe Ia and is by far the most well-studied photometrically transitional and spectroscopically 91bg-like SN to date. The high-cadence observations of SN 2022xkq offer a detailed view of its photometric and spectroscopic evolution, in particular the early light curve and carbon features. The early multiband light curve of SN 2022xkq reveals a possible flux excess that is most prominent in the redder bands. To our knowledge, SN 2022xkq is the first transitional/91bg-like SN Ia with multiband observations soon enough after explosion to detect the presence of an early excess. Multiband photometry within days of explosion of more transitional/91bg-like SNe is crucial to understanding whether the red color in SN 2022xkq is unique or typical of this subclass of SNe Ia.

SN 2022xkq is another member of the increasing sample of transitional/91bg-like SNe Ia that exhibit strong carbon features, in both the optical and infrared. The spectroscopic data set presented in this paper offers near-complete coverage of the evolution of the C II λ6580 and C I λ10693 lines. The NIR data set collected for this SN is the most complete C I evolution observed to date and will be invaluable for understanding the processes that produce carbon-rich SNe Ia.

No current model of any explosion scenario predicts a red excess and early light curve like those exhibited in SN 2022xkq. Red excesses are often linked to double-detonation mechanisms. However, the overall light-curve shape and color, as well as the strong C lines of SN 2022xkq, do not agree with existing double-detonation models. Other scenarios predicted to produce early flux excesses, including companion shocking, nontypical nickel distribution, and mergers, are unable to describe both the color and shape of the pre-maximum light curve as well.

Spectroscopically, SN 2022xkq is not particularly well described by the models we consider either. The spectra are closer to modeled spectra of the detonation of a pure sub-Chandrasekhar mass white dwarf when compared to models of delayed detonation. However, models currently suggest that sub-Chandrasekhar mass progenitors, for both pure and double detonation, do not produce the strong and persistent carbon features observed in SN 2022xkq. The evolution of the line we identify as C I could be produced by He I in a sub-Chandrasekhar double-detonation scenario (Collins et al. 2023), though we do not detect any other expected He I lines despite obtaining spectra less than 48 hr after explosion. In contrast, delayed-detonation models have been shown to better explain the carbon evolution but do not explain the weaker Sc II/Ti II absorption trough at 4000–4200 Å in the early spectra of SN 2022xkq.

No current publicly available model can explain the early color and light curve, the spectroscopic evolution, and the strength of the carbon features of SN 2022xkq all at once. Given the breadth of the observational record available, this SN offers the unique opportunity to rigorously test progenitor scenarios. SN 2022xkq will be an important reference point in our efforts to understand the progenitors and explosions of underluminous SNe Ia.

Acknowledgments

Time-domain research by the University of Arizona team, J.P., and D.J.S. is supported by NSF grants AST-1821987, 1813466, 1908972, 2108032, and 2308181 and by the Heising-Simons Foundation under grant No. 2020-1864.

P.L. acknowledges support from the Swedish Research Council.

L.G. acknowledges financial support from the Spanish Ministerio de Ciencia e Innovación (MCIN), the Agencia Estatal de Investigación (AEI) 10.13039/501100011033, and the European Social Fund (ESF) "Investing in your future" under the 2019 Ramón y Cajal program RYC2019-027683-I and the PID2020-115253GA-I00 HOSTFLOWS project; from Centro Superior de Investigaciones Científicas (CSIC) under

the PIE project 20215AT016; and from the program Unidad de Excelencia María de Maeztu CEX2020-001058-M.

This publication was made possible through the support of an LSSTC Catalyst Fellowship to K.A.B., funded through grant 62192 from the John Templeton Foundation to LSST Corporation. The opinions expressed in this publication are those of the authors and do not necessarily reflect the views of LSSTC or the John Templeton Foundation.

Research by Y.D., S.V., N.M.R, E.H., and D.M. is supported by NSF grant AST-2008108.

The Keck Infrared Transient Survey was executed primarily by members of the UC Santa Cruz transients team, who were supported in part by NASA grants NNG17PX03C, 80NSSC21K2076, 80NSSC22K1513, and 80NSSC22K1518; by NSF grant AST–1911206; and by fellowships from the Alfred P. Sloan Foundation and the David and Lucile Packard Foundation to R.J.F. KITS was directly supported by NASA grant 80NSSC23K0301.

S.B.'s work was supported by the "Programme National de Physique Stellaire" (PNPS) of CNRS/INSU, co-funded by CEA and CNES, and has made use of computing facilities operated by CeSAM data center at LAM, Marseille, France.

M.N. is supported by the European Research Council (ERC) under the European Union's Horizon 2020 research and innovation program (grant agreement No. 948381) and by UK Space Agency grant No. ST/Y000692/1.

This work was funded in part by ANID, Millennium Science Initiative, ICN12_009.

J.S. acknowledges support from the Packard Foundation.

Y.-Z.C. is supported by the National Natural Science Foundation of China (NSFC, grant No. 12303054) and the International Centre of Supernovae, Yunnan Key Laboratory (No. 202302AN360001).

I.S. is supported by funding from the Italian Ministry of Education, University and Research (MIUR), PRIN 2017 (grant 20179ZF5KS), and PRIN-INAF 2022 project "Shedding light on the nature of gap transients: from the observations to the models" and acknowledges the support of the doctoral grant funded by Istituto Nazionale di Astrofisica via the University of Padova and MIUR.

The SALT data presented here were obtained via Rutgers University program 2022-1-MLT-004 (PI: S.W.J.).

L.A.K. acknowledges support by NASA FINESST fellowship 80NSSC22K1599.

C.L. acknowledges support from the National Science Foundation Graduate Research Fellowship under grant No. DGE-2233066.

M.M. acknowledges support in part from ADAP program grant No. 80NSSC22K0486, from the NSF AST-2206657, and from the HST GO program HST-GO-16656.

L.C. is grateful for support from NSF grants AST-2107070 and AST-2205628.

This work was performed in part at the Aspen Center for Physics, which is supported by National Science Foundation grant PHY-2210452.

The Australia Telescope Compact Array is part of the Australia Telescope National Facility,[58] which is funded by the Australian Government for operation as a National Facility managed by CSIRO. We acknowledge the Gomeroi people as the traditional owners of the Observatory site. The ATCA data reported here were obtained under Program C1473 (P.I. S. Ryder).

The Las Cumbres Observatory group is supported by NSF grants AST-1911151 and AST-1911225.

This research has made use of the NASA Astrophysics Data System (ADS) Bibliographic Services, and the NASA/IPAC Extragalactic Database (NED), which is operated by the Jet Propulsion Laboratory, California Institute of Technology, under contract with the National Aeronautics and Space Administration.

This paper uses observations made with the MuSCAT3 instrument, developed by the Astrobiology Center and under financial supports by JSPS KAKENHI (JP18H05439) and JST PRESTO (JPMJPR1775), at Faulkes Telescope North on Maui, HI, operated by the Las Cumbres Observatory.

Some observations reported here were obtained at the MMT Observatory, a joint facility of the University of Arizona and the Smithsonian Institution.

This work includes observations obtained at the Southern Astrophysical Research (SOAR) telescope, which is a joint project of the Ministério da Ciência, Tecnologia e Inovações (MCTI/LNA) do Brasil, the US National Science Foundation's NOIRLab, the University of North Carolina at Chapel Hill (UNC), and Michigan State University (MSU).

The LBT is an international collaboration among institutions in the United States, Italy, and Germany. LBT Corporation Members are: the University of Arizona on behalf of the Arizona Board of Regents; Istituto Nazionale di Astrofisica, Italy; LBT Beteiligungsgesellschaft, Germany, representing the Max-Planck Society, the Leibniz Institute for Astrophysics Potsdam, and Heidelberg University; The Ohio State University; and the Research Corporation, on behalf of the University of Notre Dame, University of Minnesota, and University of Virginia. This paper made use of the modsCCDRed data reduction code developed in part with funds provided by NSF grants AST-9987045 and AST-1108693.

The data presented here were obtained in part with ALFOSC, which is provided by the Instituto de Astrofisica de Andalucia (IAA) under a joint agreement with the University of Copenhagen and NOT.

This work has made use of data from the Asteroid Terrestrial-impact Last Alert System (ATLAS) project. The Asteroid Terrestrial-impact Last Alert System (ATLAS) project is primarily funded to search for near-Earth asteroids through NASA grants NN12AR55G, 80NSSC18K0284, and 80NSSC18K1575; by-products of the NEO search include images and catalogs from the survey area. This work was partially funded by Kepler/K2 grant J1944/80NSSC19K0112, HST GO-15889, and STFC grants ST/T000198/1 and ST/S006109/1. The ATLAS science products have been made possible through the contributions of the University of Hawaii Institute for Astronomy, the Queen's University Belfast, the Space Telescope Science Institute, the South African Astronomical Observatory, and the Millennium Institute of Astrophysics (MAS), Chile.

This work includes data obtained with the Swope Telescope at Las Campanas Observatory, Chile, as part of the Swope Time Domain Key Project (PI: Piro; Co-Is: Coulter, Drout, Phillips, Holoien, French, Cowperthwaite, Burns, Madore, Foley, Kilpatrick, Rojas-Bravo, Dimitriadis, Hsiao). We thank Abdo Campillay and Yilin Kong-Riveros for observations on the Swope Telescope.

[58] https://ror.org/05qajvd42

A major upgrade of the Kast spectrograph on the Shane 3 m telescope at Lick Observatory was made possible through generous gifts from the Heising-Simons Foundation and William and Marina Kast. Research at Lick Observatory is partially supported by a generous gift from Google.

NASA Keck time is administered by the NASA Exoplanet Science Institute. Data presented herein were obtained at the W. M. Keck Observatory from telescope time allocated to the National Aeronautics and Space Administration through the agency's scientific partnership with the California Institute of Technology and the University of California. The Observatory was made possible by the generous financial support of the W. M. Keck Foundation. The authors wish to recognize and acknowledge the very significant cultural role and reverence that the summit of Maunakea has always had within the indigenous Hawaiian community. We are most fortunate to have the opportunity to conduct observations from this mountain.

Facilities: ADS, ATCA, CTIO:PROMPT, LBT (MODS), Las Cumbres Observatory (Sinistro, FLOYDS), Keck I (LRIS), Keck II (NIRES), NED, SALT (RSS), SOAR (GHTS, TripleSpec), Lick Shane (Kast), WISeREP, USASK:PROMPT

Software: AIPS (Wells 1985), astropy (Astropy Collaboration et al. 2013, 2018), `AutoPhOT` (Brennan & Fraser 2022), Binospec pipeline (Kansky et al. 2019), CASA (McMullin et al. 2007), CMFGEN (Hillier & Miller 1998; Hillier & Dessart 2012), corner (Foreman-Mackey 2016), emcee (Foreman-Mackey et al. 2013), FLOYDS pipeline (Valenti et al. 2014), HEASoft (NASA High Energy Astrophysics Science Archive Research Center (Heasarc), 2014), `HOTPANTS` (Becker 2015), IDSRED (Müller Bravo 2023), `lcogtsnpipe` (Valenti et al. 2016), Light Curve Fitting (Hosseinzadeh & Gomez 2020), MatPLOTLIB (Hunter 2007), MIRIAD (Sault et al. 1995), modsCCDRed (Pogge 2019), NumPy (Harris et al. 2020), PESSTO pipeline (Smartt et al. 2015), `photpipe` (Rest et al. 2005), Photutils (Bradley et al. 2022), PyEmir (Pascual et al. 2010; Cardiel et al. 2019), PyNOT-redux (https://pypi.org/project/PyNOT-redux/), PypeIt (Prochaska et al. 2020b, 2020a), PySALT (Crawford et al. 2010), Scipy (Virtanen et al. 2020), SNIFS pipeline (Tucker et al. 2022), `SNooPy` (Burns et al. 2011), `Spextool` (Cushing et al. 2004), `UCSC Spectral Pipeline` (Siebert et al. 2019), WISeREP (Yaron & Gal-Yam 2012), `YSE-PZ` (Coulter et al. 2022, 2023).

Appendix

Table 3 shows the complete spectroscopic log, both optical and NIR, of observations of SN 2022xkq reported in this work. All spectra are available on WISeRep.[59]

Table 3
Log of Spectroscopic Observations

Date (UTC)	JD	Epoch (days)[a]	Telescope	Instrument	Range (Å)	Exp (s)	Slit (arcsec)
2022-10-13	2459865.938	−13.6	P60	SEDM	3780–9220	1800	IFU
2022-10-13	2459866.496	−13.0	SALT	RSS	3930–8600	1980	1.50
2022-10-15	2459867.833	−11.7	ESO-NTT	EFOSC2-NTT	3670–9270	2700	1.0
2022-10-15	2459868.022	−11.5	FTN	FLOYDS	3500–10,000	3600	2
2022-10-15	2459868.041	−11.5	Keck	NIRES	9410–24,690	1000	0.55
2022-10-16	2459868.666	−10.9	ESO-NTT	EFOSC2-NTT	3370–7490	1800	1.0
2022-10-16	2459868.692	−10.9	ESO-NTT	SOFI	9380–16,480	3240	1
2022-10-16	2459868.753	−10.8	Baade	IMACS	4200–9390	900	0.7
2022-10-16	2459868.782	−10.8	ESO-NTT	EFOSC2-NTT	6020–10,010	1800	1.0
2022-10-17	2459869.571	−10.0	NOT	ALFOSC	3400–9610	1800	1.3
2022-10-17	2459869.674	−9.9	SOAR	GHTS RED	3650–7000	1800	1.0
2022-10-17	2459869.816	−9.7	P60	SEDM	3780–9220	1800	IFU
2022-10-17	2459870.07	−9.5	FTN	FLOYDS	3500–10,000	3600	2
2022-10-18	2459870.669	−8.9	ESO-NTT	SOFI	9380–16,480	3240	1
2022-10-18	2459870.878	−8.7	Bok	B&C	4100–8000	4500	1.50
2022-10-18	2459871.484	−8.1	SALT	RSS	3920–8600	1980	1.50
2022-10-19	2459871.8	−7.8	Bok	B&C	4870–6020	7500	1.50
2022-10-19	2459872.019	−7.6	UH88	SNIFS	3400–9100	1800	IFU
2022-10-19	2459872.489	−7.1	SALT	RSS	3920–8600	1980	1.50
2022-10-20	2459872.876	−6.7	Bok	B&C	4000–8000	6000	1.50
2022-10-20	2459873.071	−6.5	FTN	FLOYDS	3500–10,000	2100	2
2022-10-21	2459873.68	−5.9	SOAR	TripleSpec	9400–24,660	300	1.0
2022-10-21	2459874.093	−5.5	FTN	FLOYDS	3800–10,000	1800	2
2022-10-22	2459874.57	−5.0	NOT	ALFOSC	3440–10,260	900	1.0
2022-10-22	2459875.074	−4.5	UH88	SNIFS	3400–9100	1800	IFU
2022-10-22	2459875.142	−4.5	Keck	LRIS	3160–10,150	250	1
2022-10-24	2459876.605	−3.0	NOT	ALFOSC	3400-9660	900	1.3
2022-10-24	2459877.043	−2.6	FTN	FLOYDS	3500–10,000	1800	2
2022-10-26	2459878.718	−0.9	SOAR	GHTS RED	4980–8990	600	1.0
2022-10-26	2459879.051	−0.6	UH88	SNIFS	3400–9100	1800	IFU
2022-10-27	2459879.74	0.1	SOAR	GHTS BLUE	3700–7120	600	1.0
2022-10-27	2459879.743	0.1	GTC	EMIR	8900–23,000	480	0.8
2022-10-27	2459879.779	0.1	SOAR	TripleSpec	9400–24,660	180	1.1

[59] https://www.wiserep.org

Table 3
(Continued)

Date (UTC)	JD	Epoch (days)[a]	Telescope	Instrument	Range (Å)	Exp (s)	Slit (arcsec)
2022-10-28	2459880.822	1.2	LBT	MODS1	3630–10,000	1800	1
2022-10-28	2459880.938	1.3	Shane	Kast	3250–10750	600	2.0
2022-10-29	2459881.928	2.3	ARC	KOSMOS	3900–9200	400	2.10
2022-10-29	2459882.46	2.8	SALT	RSS	3920–8600	1980	1.50
2022-10-30	2459882.781	3.1	SOAR	GHTS RED	4000–7910	1200	1.0
2022-10-30	2459883.141	3.5	FTS	FLOYDS	3500–10,000	900	2
2022-10-31	2459883.55	3.9	NOT	ALFOSC	3420–9700	900	1.0
2022-10-31	2459883.787	4.1	ESO-NTT	EFOSC	3650–9250	1080	1.5
2022-10-31	2459884.019	4.3	UH88	SNIFS	3400–9100	1800	IFU
2022-11-01	2459884.788	5.1	ESO-NTT	SOFI	9380–16,480	960	1
2022-11-02	2459886.047	6.4	FTS	FLOYDS	3500–10,000	900	2
2022-11-04	2459887.526	7.8	INT	IDS	3800–9000	1500	0.974
2022-11-04	2459887.882	8.2	Shane	Kast	3250–10,890	600	2.0
2022-11-05	2459888.501	8.8	INT	IDS	3800–9000	1200	0.974
2022-11-05	2459888.626	8.9	GTC	EMIR	8900–23,000	480	0.8
2022-11-05	2459889.071	9.4	FTS	FLOYDS	3500–10,000	900	2
2022-11-06	2459889.711	10.0	INT	IDS	3600–9000	1200	0.974
2022-11-06	2459890.005	10.3	Keck	NIRES	9410–24,690	800	0.55
2022-11-07	2459890.586	10.9	INT	IDS	3800–9000	1500	1.488
2022-11-09	2459893.428	13.7	SALT	RSS	3920–8600	1980	1.50
2022-11-10	2459894.02	14.3	FTS	FLOYDS	3500–10,000	899	2
2022-11-10	2459894.424	14.7	SALT	RSS	3920–8600	1980	1.50
2022-11-13	2459896.61	16.8	NOT	ALFOSC	3400-9630	900	1.3
2022-11-13	2459897.415	17.6	SALT	RSS	3920–8600	1980	1.50
2022-11-14	2459897.743	18.0	SOAR	TripleSpec	9400–24,660	300	1.0
2022-11-15	2459899.029	19.2	UH88	SNIFS	3400–9100	2200	IFU
2022-11-16	2459899.874	20.1	Bok	B&C	3940–8250	6000	1.50
2022-11-16	2459899.948	20.2	UH88	SNIFS	3400–9100	1800	IFU
2022-11-16	2459899.966	20.2	FTS	FLOYDS	3500–10,000	900	2
2022-11-17	2459901.005	21.2	Keck	NIRES	9410–24,690	480	0.55
2022-11-17	2459901.403	21.6	SALT	RSS	3920–8600	1980	1.50
2022-11-18	2459901.812	22.0	ESO-NTT	SOFI	9380–16,480	960	1
2022-11-18	2459901.92	22.1	Bok	B&C	4900–6000	7500	1.50
2022-11-21	2459904.841	25.0	Shane	Kast	3250–10,690	600	2.0
2022-11-22	2459905.679	25.8	SOAR	TripleSpec	9400–24,660	300	1.0
2022-11-23	2459907.019	27.2	FTS	FLOYDS	3500–10,000	899	2
2022-11-27	2459910.994	31.1	UH88	SNIFS	3400–9100	2400	IFU
2022-11-28	2459911.545	31.7	NOT	ALFOSC	3400–9710	900	1.0
2022-11-28	2459911.686	31.8	SOAR	GHTS RED	4960–8970	600	1.0
2022-11-29	2459912.587	32.7	SOAR	TripleSpec	9400–24,660	300	1.0
2022-11-29	2459912.683	32.8	SOAR	GHTS BLUE	3750–7110	600	1.0
2022-11-29	2459913.056	33.2	FTS	FLOYDS	3500–10,000	900	2
2022-12-03	2459916.988	37.1	FTS	FLOYDS	3500–10,000	900	2
2022-12-06	2459920.361	40.4	SALT	RSS	3920–8600	1910	1.50
2022-12-12	2459925.599	45.6	SOAR	GHTS RED	4950–8960	1800	1.0
2022-12-13	2459926.558	46.6	INT	IDS	3800–9000	1800	1.001
2022-12-14	2459927.902	47.9	FTN	FLOYDS	3500–10,000	900	2
2022-12-15	2459928.761	48.7	Bok	B&C	4000–8000	7500	1.50
2022-12-17	2459930.536	50.5	GTC	EMIR	8900–23,000	1440	0.8
2022-12-19	2459932.772	52.7	MMT	Binospec	5260–7750	3600	1
2022-12-21	2459934.644	54.6	SOAR	GHTS RED	4960–8960	1800	1.0
2022-12-21	2459934.751	54.7	ESO-NTT	SOFI	9380–16,480	2970	1
2022-12-21	2459934.806	54.7	Shane	Kast	3250–10,890	1200	2.0
2022-12-24	2459937.838	57.8	ARC	KOSMOS	3780–9650	1800	2.10
2022-12-24	2459938.138	58.0	FTS	FLOYDS	5050–10,000	2700	2
2022-12-29	2459942.691	62.6	ESO-NTT	EFOSC	3360–7480	1800	1.5
2022-12-29	2459942.691	62.6	ESO-NTT	EFOSC	6000–10,010	1800	1.5
2022-12-31	2459944.971	64.8	Keck	NIRES	9410–24,690	1200	0.55
2023-01-05	2459950.398	70.2	GTC	EMIR	8900–23,000	1440	0.8
2023-01-07	2459952.451	72.3	SALT	RSS	3920–8600	1980	1.50
2023-01-11	2459955.72	75.5	SOAR	GHTS RED	4920–8930	1800	1.0
2023-01-13	2459957.646	77.4	MMT	Binospec	5260–7750	3600	1
2023-01-13	2459957.655	77.4	ESO-NTT	EFOSC	3360–7480	1800	1.5
2023-01-13	2459957.679	77.4	ESO-NTT	EFOSC	6000–10,000	1800	1.5

Table 3
(Continued)

Date (UTC)	JD	Epoch (days)[a]	Telescope	Instrument	Range (Å)	Exp (s)	Slit (arcsec)
2023-01-14	2459958.998	78.7	FTS	FLOYDS	3500–10,000	2700	2
2023-01-25	2459970.452	90.1	GTC	OSIRIS	3630–7790	800	1.0
2023-01-25	2459970.452	90.1	GTC	OSIRIS	5100–10,300	800	1.0
2023-01-26	2459970.592	90.3	SOAR	GHTS RED	4920–8930	1800	1.0
2023-01-27	2459971.757	91.4	Shane	Kast	3250–10740	2400	2.0
2023-01-31	2459976.388	96.0	SALT	RSS	3920–8600	1980	1.50
2023-02-01	2459977.001	96.6	FTS	FLOYDS	3500–10,000	2700	2
2023-02-08	2459983.819	103.4	Keck	NIRES	9410–24,690	2400	0.55
2023-02-11	2459987.346	106.9	SALT	RSS	6140–6940	2400	1.50
2023-02-23	2459998.551	118.0	Clay	LDSS-3	3900–10,630	900	1.0
2023-02-24	2459999.941	119.4	FTS	FLOYDS	3500–10,000	3600	2
2023-03-05	2460008.582	128.0	Baade	IMACS	4200–9380	1200	0.7
2023-03-14	2460017.892	137.2	FTS	FLOYDS	3500–10,000	3600	2
2023-03-30	2460033.507	152.7	SOAR	GHTS RED	4930–8930	3600	1.0

Note.
[a] Relative to B_{max}.

ORCID iDs

Jeniveve Pearson https://orcid.org/0000-0002-0744-0047
David J. Sand https://orcid.org/0000-0003-4102-380X
Peter Lundqvist https://orcid.org/0000-0002-3664-8082
Lluís Galbany https://orcid.org/0000-0002-1296-6887
Jennifer E. Andrews https://orcid.org/0000-0003-0123-0062
K. Azalee Bostroem https://orcid.org/0000-0002-4924-444X
Yize Dong (董一泽) https://orcid.org/0000-0002-7937-6371
Emily Hoang https://orcid.org/0000-0003-2744-4755
Griffin Hosseinzadeh https://orcid.org/0000-0002-0832-2974
Daryl Janzen https://orcid.org/0000-0003-0549-3281
Jacob E. Jencson https://orcid.org/0000-0001-5754-4007
Michael J. Lundquist https://orcid.org/0000-0001-9589-3793
Nicolás Meza Retamal https://orcid.org/0000-0002-7015-3446
Manisha Shrestha https://orcid.org/0000-0002-4022-1874
Stefano Valenti https://orcid.org/0000-0001-8818-0795
Samuel Wyatt https://orcid.org/0000-0003-2732-4956
Joseph P. Anderson https://orcid.org/0000-0003-0227-3451
Chris Ashall https://orcid.org/0000-0002-5221-7557
Katie Auchettl https://orcid.org/0000-0002-4449-9152
Eddie Baron https://orcid.org/0000-0001-5393-1608
Stéphane Blondin https://orcid.org/0000-0002-9388-2932
Christopher R. Burns https://orcid.org/0000-0003-4625-6629
Yongzhi Cai (蔡永志) https://orcid.org/0000-0002-7714-493X
Ting-Wan Chen https://orcid.org/0000-0002-1066-6098
Laura Chomiuk https://orcid.org/0000-0002-8400-3705
David A. Coulter https://orcid.org/0000-0003-4263-2228
Kyle W. Davis https://orcid.org/0000-0002-5680-4660
Thomas de Jaeger https://orcid.org/0000-0001-6069-1139
James M. DerKacy https://orcid.org/0000-0002-7566-6080
Dhvanil D. Desai https://orcid.org/0000-0002-2164-859X
Georgios Dimitriadis https://orcid.org/0000-0001-9494-179X
Aaron Do https://orcid.org/0000-0003-3429-7845
Joseph R. Farah https://orcid.org/0000-0003-4914-5625
Ryan J. Foley https://orcid.org/0000-0002-2445-5275
Mariusz Gromadzki https://orcid.org/0000-0002-1650-1518
Claudia P. Gutiérrez https://orcid.org/0000-0003-2375-2064
Joshua Haislip https://orcid.org/0000-0002-6703-805X
Jonay I. González Hernández https://orcid.org/0000-0002-0264-7356
Jason T. Hinkle https://orcid.org/0000-0001-9668-2920
Willem B. Hoogendam https://orcid.org/0000-0003-3953-9532
D. Andrew Howell https://orcid.org/0000-0003-4253-656X
Peter Hoeflich https://orcid.org/0000-0002-4338-6586
Eric Hsiao https://orcid.org/0000-0003-1039-2928
Mark E. Huber https://orcid.org/0000-0003-1059-9603
Saurabh W. Jha https://orcid.org/0000-0001-8738-6011
Cristina Jiménez Palau https://orcid.org/0000-0002-4374-0661
Charles D. Kilpatrick https://orcid.org/0000-0002-5740-7747
Vladimir Kouprianov https://orcid.org/0000-0003-3642-5484
Sahana Kumar https://orcid.org/0000-0001-8367-7591
Lindsey A. Kwok https://orcid.org/0000-0003-3108-1328
Conor Larison https://orcid.org/0000-0003-2037-4619
Natalie LeBaron https://orcid.org/0000-0002-2249-0595
Xavier Le Saux https://orcid.org/0009-0004-3242-282X
Jing Lu https://orcid.org/0000-0002-3900-1452
Curtis McCully https://orcid.org/0000-0001-5807-7893
Tycho Mera Evans https://orcid.org/0000-0001-5888-2542
Peter Milne https://orcid.org/0000-0002-0370-157X
Maryam Modjaz https://orcid.org/0000-0001-7132-0333
Nidia Morrell https://orcid.org/0000-0003-2535-3091
Tomás E. Müller-Bravo https://orcid.org/0000-0003-3939-7167
Megan Newsome https://orcid.org/0000-0001-9570-0584
Matt Nicholl https://orcid.org/0000-0002-2555-3192
Estefania Padilla Gonzalez https://orcid.org/0000-0003-0209-9246
Anna V. Payne https://orcid.org/0000-0003-3490-3243
Craig Pellegrino https://orcid.org/0000-0002-7472-1279
Kim Phan https://orcid.org/0000-0001-6383-860X
Jonathan Pineda-García https://orcid.org/0000-0003-0737-8463
Anthony L. Piro https://orcid.org/0000-0001-6806-0673
Lara Piscarreta https://orcid.org/0009-0006-4637-4085
Abigail Polin https://orcid.org/0000-0002-1633-6495
Daniel E. Reichart https://orcid.org/0000-0002-5060-3673
César Rojas-Bravo https://orcid.org/0000-0002-7559-315X
Stuart D. Ryder https://orcid.org/0000-0003-4501-8100
Irene Salmaso https://orcid.org/0000-0003-1450-0869
Michaela Schwab https://orcid.org/0009-0002-5096-1689
Melissa Shahbandeh https://orcid.org/0000-0002-9301-5302

Benjamin J. Shappee https://orcid.org/0000-0003-4631-1149
Matthew R. Siebert https://orcid.org/0000-0003-2445-3891
Nathan Smith https://orcid.org/0000-0001-5510-2424
Jay Strader https://orcid.org/0000-0002-1468-9668
Kirsty Taggart https://orcid.org/0000-0002-5748-4558
Giacomo Terreran https://orcid.org/0000-0003-0794-5982
Samaporn Tinyanont https://orcid.org/0000-0002-1481-4676
M. A. Tucker https://orcid.org/0000-0002-2471-8442
Giorgio Valerin https://orcid.org/0000-0002-3334-4585
D. R. Young https://orcid.org/0000-0002-1229-2499

References

Aleo, P. D., Malanchev, K., Sharief, S., et al. 2023, ApJS, 266, 9
Arnett, W. D. 1982, ApJ, 253, 785
Arnett, W. D., Branch, D., & Wheeler, J. C. 1985, Natur, 314, 337
Ashall, C., Hsiao, E. Y., Hoeflich, P., et al. 2019, ApJL, 875, L14
Ashall, C., Lu, J., Shappee, B. J., et al. 2022, ApJL, 932, L2
Ashall, C., Mazzali, P. A., Pian, E., & James, P. A. 2016, MNRAS, 463, 1891
Ashall, C., Mazzali, P. A., Stritzinger, M. D., et al. 2018, MNRAS, 477, 153
Astropy Collaboration, Price-Whelan, A. M., Sipőcz, B. M., et al. 2018, AJ, 156, 123
Astropy Collaboration, Robitaille, T. P., Tollerud, E. J., et al. 2013, A&A, 558, A33
Becker, A., 2015 HOTPANTS: High Order Transform of PSF ANd Template Subtraction, Astrophysics Source Code Library, ascl:1504.004
Bellm, E. C., Kulkarni, S. R., Graham, M. J., et al. 2019, PASP, 131, 018002
Björnsson, C. I., & Lundqvist, P. 2014, ApJ, 787, 143
Blagorodnova, N., Neill, J. D., Walters, R., et al. 2018, PASP, 130, 035003
Blondin, S., Dessart, L., & Hillier, D. J. 2018, MNRAS, 474, 3931
Blondin, S., Dessart, L., Hillier, D. J., & Khokhlov, A. M. 2013, MNRAS, 429, 2127
Blondin, S., Dessart, L., Hillier, D. J., & Khokhlov, A. M. 2017, MNRAS, 470, 157
Blondin, S., Dessart, L., Hillier, D. J., & Khokhlov, A. M. 2023, Evidence for Sub-Chandrasekhar-mass Progenitors of Type Ia Supernovae at the Faint End of the Width-Luminosity Relation, Zenodo, doi:10.5281/zenodo.8379254
Blondin, S., Matheson, T., Kirshner, R. P., et al. 2012, AJ, 143, 126
Boehner, P., Plewa, T., & Langer, N. 2017, MNRAS, 465, 2060
Botyánszki, J., Kasen, D., & Plewa, T. 2018, ApJL, 852, L6
Boyle, A., Sim, S. A., Hachinger, S., & Kerzendorf, W. 2017, A&A, 599, A46
Bradley, L., Sipőcz, B., Robitaille, T., et al. 2022, astropy/photutils: v1.6.0, Zenodo, doi:10.5281/zenodo.7419741
Branch, D., Dang, L. C., Hall, N., et al. 2006, PASP, 118, 560
Breeveld, A. A., Landsman, W., Holland, S. T., et al. 2011, in AIP Conf. Ser. 1358, Gamma Ray Bursts 2010, ed. J. E. McEnery, J. L. Racusin, & N. Gehrels (Melville, NY: AIP), 373
Brennan, S. J., & Fraser, M. 2022, A&A, 667, A62
Brown, T. M., Baliber, N., Bianco, F. B., et al. 2013, PASP, 125, 1031
Bulla, M., Miller, A. A., Yao, Y., et al. 2020, ApJ, 902, 48
Burke, J., Howell, D. A., Sand, D. J., & Hosseinzadeh, G. 2022a, arXiv:2208.11201
Burke, J., Howell, D. A., Sand, D. J., et al. 2022b, arXiv:2207.07681
Burke, J., Howell, D. A., Sarbadhicary, S. K., et al. 2021, ApJ, 919, 142
Burns, C. R., Parent, E., Phillips, M. M., et al. 2018, ApJ, 869, 56
Burns, C. R., Stritzinger, M., Phillips, M. M., et al. 2011, AJ, 141, 19
Burns, C. R., Stritzinger, M., Phillips, M. M., et al. 2014, ApJ, 789, 32
Burrow, A., Baron, E., Ashall, C., et al. 2020, ApJ, 901, 154
Buzzoni, B., Delabre, B., Dekker, H., et al. 1984, Msngr, 38, 9
Cardiel, N., Pascual, S., Gallego, J., et al. 2019, in ASP Conf. Ser. 523, Astronomical Data Analysis Software and Systems XXVII, ed. P. J. Teuben et al. (San Francisco, CA: ASP), 317
Cepa, J., Aguiar, M., Escalera, V. G., et al. 2000, Proc. SPIE, 4008, 623
Cepa, J., Aguiar-Gonzalez, M., Bland-Hawthorn, J., et al. 2003, Proc. SPIE, 4841, 1739
Chen, P., Bruch, R., Zimmerman, E., et al. 2022a, TNSCR 2975, 1
Chen, P., Schulze, S., Sollerman, J., & Maguire, K. 2022b, TNSCR 3026, 1
Chen, T. W., Yang, S., Pan, Y. C., et al. 2021, TNSAN, 92, 1
Chevalier, R. A., & Fransson, C. 2006, ApJ, 651, 381
Chomiuk, L., Soderberg, A. M., Chevalier, R. A., et al. 2016, ApJ, 821, 119
Chomiuk, L., Soderberg, A. M., Moe, M., et al. 2012, ApJ, 750, 164
Clemens, J. C., Crain, J. A., & Anderson, R. 2004, Proc. SPIE, 5492, 331
Collins, C. E., Sim, S. A., Shingles, L. J., et al. 2023, MNRAS, 524, 4447
Conley, A., Howell, D. A., Howes, A., et al. 2006, AJ, 132, 1707
Conley, A., Sullivan, M., Hsiao, E. Y., et al. 2008, ApJ, 681, 482
Coulter, D. A., Jones, D. O., McGill, P., et al. 2022, YSE-PZ: An Open-source Target and Observation Management System, v0.3.0, Zenodo, doi:10.5281/zenodo.7278430
Coulter, D. A., Jones, D. O., McGill, P., et al. 2023, PASP, 135, 064501
Crawford, S. M., Still, M., Schellart, P., et al. 2010, Proc. SPIE, 7737, 773725
Cristiani, S., Cappellaro, E., Turatto, M., et al. 1992, A&A, 259, 63
Cushing, M. C., Vacca, W. D., & Rayner, J. T. 2004, PASP, 116, 362
De, K., Kasliwal, M. M., Polin, A., et al. 2019, ApJL, 873, L18
de Vaucouleurs, G., de Vaucouleurs, A., Corwin, H. G. J., et al. 1991, Third Reference Catalogue of Bright Galaxies (Berlin: Springer)
Deckers, M., Maguire, K., Magee, M. R., et al. 2022, MNRAS, 512, 1317
Desai, D. D., Kochanek, C. S., Shappee, B. J., et al. 2023, arXiv:2306.11100
Dessart, L., Blondin, S., Hillier, D. J., & Khokhlov, A. 2014, MNRAS, 441, 532
Dessart, L., Leonard, D. C., & Prieto, J. L. 2020, A&A, 638, A80
Dhawan, S., Leibundgut, B., Spyromilio, J., & Blondin, S. 2017, A&A, 602, A118
di Serego-Alighieri, S., & Ponz, J. D. 1987, in ESO Conf. and Workshop Proc. 26, ed. I.J. Danziger (Garching: ESO), 545
Di Stefano, R., Voss, R., & Claeys, J. S. W. 2011, ApJL, 738, L1
Dimitriadis, G., Foley, R. J., Rest, A., et al. 2019, ApJL, 870, L1
Dong, Y., Valenti, S., Polin, A., et al. 2022, ApJ, 934, 102
Dressler, A., Bigelow, B., Hare, T., et al. 2011, PASP, 123, 288
Elias-Rosa, N., Chen, P., Benetti, S., et al. 2021, A&A, 652, A115
Erwin, P., & Debattista, V. P. 2013, MNRAS, 431, 3060
Fabricant, D., Fata, R., Epps, H., et al. 2019, PASP, 131, 075004
Fausnaugh, M. M., Vallely, P. J., Tucker, M. A., et al. 2023, ApJ, 956, 108
Filippenko, A. V., Richmond, M. W., Branch, D., et al. 1992, AJ, 104, 1543
Fink, M., Röpke, F. K., Hillebrandt, W., et al. 2010, A&A, 514, A53
Firth, R. E., Sullivan, M., Gal-Yam, A., et al. 2015, MNRAS, 446, 3895
Flewelling, H. A., Magnier, E. A., Chambers, K. C., et al. 2020, ApJS, 251, 7
Folatelli, G., Phillips, M. M., Burns, C. R., et al. 2010, AJ, 139, 120
Folatelli, G., Phillips, M. M., Morrell, N., et al. 2012, ApJ, 745, 74
Foreman-Mackey, D. 2016, JOSS, 1, 24
Foreman-Mackey, D., Hogg, D. W., Lang, D., & Goodman, J. 2013, PASP, 125, 306
Galbany, L., Ashall, C., Höflich, P., et al. 2019, A&A, 630, A76
Gall, C., Stritzinger, M. D., Ashall, C., et al. 2018, A&A, 611, A58
Gallagher, J. S., Garnavich, P. M., Berlind, P., et al. 2005, ApJ, 634, 210
Ganeshalingam, M., Li, W., & Filippenko, A. V. 2011, MNRAS, 416, 2607
Garnavich, P. M., Bonanos, A. Z., Krisciunas, K., et al. 2004, ApJ, 613, 1120
Garzón, F., Balcells, M., Gallego, J., et al. 2022, A&A, 667, A107
Gehrels, N., Chincarini, G., Giommi, P., et al. 2004, ApJ, 611, 1005
Goldhaber, G., Groom, D. E., Kim, A., et al. 2001, ApJ, 558, 359
Goldstein, D. A., & Kasen, D. 2018, ApJL, 852, L33
Padilla Gonzalez, E. P., Howell, D. A., Terreran, G., et al. 2023, arXiv:2308.06334
González-Gaitán, S., Conley, A., Bianco, F. B., et al. 2012, ApJ, 745, 44
Graur, O., Bianco, F. B., Modjaz, M., et al. 2017, ApJ, 837, 121
Gronow, S., Collins, C., Ohlmann, S. T., et al. 2020, A&A, 635, A169
Gronow, S., Collins, C. E., Sim, S. A., & Röpke, F. K. 2021, A&A, 649, A155
Guy, J., Astier, P., Baumont, S., et al. 2007, A&A, 466, 11
Hamuy, M., Phillips, M. M., Suntzeff, N. B., et al. 1996, AJ, 112, 2391
Hamuy, M., Trager, S. C., Pinto, P. A., et al. 2000, AJ, 120, 1479
Harris, C. R., Millman, K. J., van der Walt, S. J., et al. 2020, Natur, 585, 357
Hayden, B. T., Garnavich, P. M., Kessler, R., et al. 2010, ApJ, 712, 350
Hillier, D. J., & Dessart, L. 2012, MNRAS, 424, 252
Hillier, D. J., & Miller, D. L. 1998, ApJ, 496, 407
Höflich, P., Gerardy, C. L., Fesen, R. A., & Sakai, S. 2002, ApJ, 568, 791
Höflich, P., Khokhlov, A. M., & Wheeler, J. C. 1995, ApJ, 444, 831
Horesh, A., Kulkarni, S. R., Fox, D. B., et al. 2012, ApJ, 746, 21
Hosseinzadeh, G., Bostroem, K. A., & Gomez, S. 2023a, Light Curve Fitting, v0.8.0, Zenodo, doi:10.5281/zenodo.7872772
Hosseinzadeh, G., & Gomez, S. 2020, Light Curve Fitting, v0.2.0, Zenodo, doi:10.5281/zenodo.4312178
Hosseinzadeh, G., Jha, S. W., Bostroem, K. A., et al. 2022a, TNSCR 2987, 1
Hosseinzadeh, G., Sand, D. J., Lundqvist, P., et al. 2022b, ApJL, 933, L45
Hosseinzadeh, G., Sand, D. J., Sarbadhicary, S. K., et al. 2023b, ApJL, 953, L15
Hosseinzadeh, G., Sand, D. J., Valenti, S., et al. 2017, ApJL, 845, L11
Howell, D. A. 2001, ApJL, 554, L193
Hoyle, F., & Fowler, W. A. 1960, ApJ, 132, 565

Hsiao, E. Y., Burns, C. R., Contreras, C., et al. 2015, A&A, 578, A9
Hunter, J. D. 2007, CSE, 9, 90
Janzen, D., Valenti, S., Bostroem, K. A., et al. 2022, TNSTR, 2022-2969, 1
Jha, S., Riess, A. G., & Kirshner, R. P. 2007, ApJ, 659, 122
Jha, S. W., Maguire, K., & Sullivan, M. 2019, NatAs, 3, 706
Jiang, J.-A., Doi, M., Maeda, K., et al. 2017, Natur, 550, 80
Jiang, J.-a., Maeda, K., Kawabata, M., et al. 2021, ApJL, 923, L8
Jones, D. O., Foley, R. J., Narayan, G., et al. 2021, ApJ, 908, 143
Justham, S. 2011, ApJL, 730, L34
Kansky, J., Chilingarian, I., Fabricant, D., et al. 2019, PASP, 131, 075005
Kasen, D. 2010, ApJ, 708, 1025
Kasen, D., Röpke, F. K., & Woosley, S. E. 2009, Natur, 460, 869
Khokhlov, A. M. 1991, A&A, 245, 114
Kilpatrick, C. D., Foley, R. J., Drout, M. R., et al. 2018, MNRAS, 473, 4805
Kollmeier, J. A., Chen, P., Dong, S., et al. 2019, MNRAS, 486, 3041
Kool, E. C., Johansson, J., Sollerman, J., et al. 2023, Natur, 617, 477
Koribalski, B. S., Staveley-Smith, L., Kilborn, V. A., et al. 2004, AJ, 128, 16
Krisciunas, K., Marion, G. H., Suntzeff, N. B., et al. 2009, AJ, 138, 1584
Kromer, M., Sim, S. A., Fink, M., et al. 2010, ApJ, 719, 1067
Kundu, E., Lundqvist, P., Pérez-Torres, M. A., Herrero-Illana, R., & Alberdi, A. 2017, ApJ, 842, 17
Lantz, B., Aldering, G., Antilogus, P., et al. 2004, Proc. SPIE, 5249, 146
Leibundgut, B., Kirshner, R. P., Phillips, M. M., et al. 1993, AJ, 105, 301
Li, W., Leaman, J., Chornock, R., et al. 2011, MNRAS, 412, 1441
Li, Z., Zhang, T., Wang, X., et al. 2022, ApJ, 927, 142
Lira, P. 1996, Master's thesis, Univ. Chile
Liu, C., Miller, A. A., Boos, S. J., et al. 2023, ApJ, 958, 178
Liu, Z.-W., Röpke, F. K., & Han, Z. 2023, RAA, 23, 082001
Lundqvist, P., Kundu, E., Pérez-Torres, M. A., et al. 2020, ApJ, 890, 159
Lundqvist, P., Mattila, S., Sollerman, J., et al. 2013, MNRAS, 435, 329
Magee, M. R., Cuddy, C., Maguire, K., et al. 2022, MNRAS, 513, 3035
Magee, M. R., & Maguire, K. 2020, A&A, 642, A189
Magee, M. R., Maguire, K., Kotak, R., et al. 2020, A&A, 634, A37
Maguire, K., Sullivan, M., Pan, Y. C., et al. 2014, MNRAS, 444, 3258
Marion, G. H., Brown, P. J., Vinkó, J., et al. 2016, ApJ, 820, 92
Martini, P., Elias, J., Points, S., et al. 2014, Proc. SPIE, 9147, 91470Z
Mazzali, P. A., Chugai, N., Turatto, M., et al. 1997, MNRAS, 284, 151
McMullin, J. P., Waters, B., Schiebel, D., Young, W., & Golap, K. 2007, in ASP Conf. Ser. 376, Astronomical Data Analysis Software and Systems XVI, ed. R. A. Shaw, F. Hill, & D. J. Bell (San Francisco, CA: ASP), 127
Miller, A. A., Cao, Y., Piro, A. L., et al. 2018, ApJ, 852, 100
Miller, A. A., Magee, M. R., Polin, A., et al. 2020a, ApJ, 898, 56
Miller, A. A., Yao, Y., Bulla, M., et al. 2020b, ApJ, 902, 47
Miller, J. S., & Stone, R. P. S. 1993, LOTRM No. 66, Lick Observatory, https://mthamilton.ucolick.org/techdocs/instruments/kast/Tech%20Report%2066%20KAST%20Miller%20Stone.pdf
Moorwood, A., Cuby, J. G., & Lidman, C. 1998, Msngr, 91, 9
Mould, J. R., Huchra, J. P., Freedman, W. L., et al. 2000, ApJ, 529, 786
Müller Bravo, T. E. 2023, temuller/idsred: First Release!, v0.1.0, Zenodo, doi:10.5281/zenodo.7851772
Munari, U., & Zwitter, T. 1997, A&A, 318, 269
NASA High Energy Astrophysics Science Archive Research Center (Heasarc), 2014 HEAsoft: Unified Release of FTOOLS and XANADU, Astrophysics Source Code Library, ascl:1408.004
Ni, Y. Q., Moon, D.-S., Drout, M. R., et al. 2022, NatAs, 6, 568
Ni, Y. Q., Moon, D.-S., Drout, M. R., et al. 2023a, ApJ, 946, 7
Ni, Y. Q., Moon, D.-S., Drout, M. R., et al. 2023b, arXiv:2304.00625
Noebauer, U. M., Kromer, M., Taubenberger, S., et al. 2017, MNRAS, 472, 2787
Nomoto, K., Thielemann, F. K., & Yokoi, K. 1984, ApJ, 286, 644
Nugent, A. E., Polin, A. E., & Nugent, P. E. 2023, arXiv:2304.10601
Oke, J. B., Cohen, J. G., Carr, M., et al. 1995, PASP, 107, 375
Olling, R. P., Mushotzky, R., Shaya, E. J., et al. 2015, Natur, 521, 332
Pakmor, R., Kromer, M., Taubenberger, S., et al. 2012, ApJL, 747, L10
Parrent, J. T., Thomas, R. C., Fesen, R. A., et al. 2011, ApJ, 732, 30
Pascual, S., Gallego, J., Cardiel, N., & Eliche-Moral, M. C. 2010, in ASP Conf. Ser. 434, Astronomical Data Analysis Software and Systems XIX, ed. Y. Mizumoto, K. I. Morita, & M. Ohishi (San Francisco, CA: ASP), 353
Pellegrino, C., Howell, D. A., Sarbadhicary, S. K., et al. 2020, ApJ, 897, 159
Pérez-Torres, M. A., Lundqvist, P., Beswick, R. J., et al. 2014, ApJ, 792, 38
Phillips, M. M. 1993, ApJL, 413, L105
Phillips, M. M. 2012, PASA, 29, 434
Phillips, M. M., Lira, P., Suntzeff, N. B., et al. 1999, AJ, 118, 1766
Phillips, M. M., Phillips, A. C., Heathcote, S. R., et al. 1987, PASP, 99, 592
Piro, A. L., & Morozova, V. S. 2016, ApJ, 826, 96
Pogge, R. 2019, rwpogge/modsCCDRed: v2.0.1, Zenodo, doi:10.5281/zenodo.2647501
Pogge, R. W., Atwood, B., Brewer, D. F., et al. 2010, Proc. SPIE, 7735, 77350A
Polin, A., Nugent, P., & Kasen, D. 2019, ApJ, 873, 84
Poznanski, D., Prochaska, J. X., & Bloom, J. S. 2012, MNRAS, 426, 1465
Prieto, J. L., Chen, P., Dong, S., et al. 2020, ApJ, 889, 100
Prochaska, J. X., Hennawi, J., Cooke, R., et al. 2020a, pypeit/PypeIt: Release v1.0.0, Zenodo, doi:10.5281/zenodo.3743493
Prochaska, J. X., Hennawi, J. F., Westfall, K. B., et al. 2020b, arXiv:2005.06505
Rest, A., Stubbs, C., Becker, A. C., et al. 2005, ApJ, 634, 1103
Richmond, M. W., & Smith, H. A. 2012, JAAVSO, 40, 872
Richmond, M. W., Treffers, R. R., Filippenko, A. V., et al. 1994, AJ, 107, 1022
Riess, A. G., Filippenko, A. V., Li, W., & Schmidt, B. P. 1999, AJ, 118, 2668
Roming, P. W. A., Kennedy, T. E., Mason, K. O., et al. 2005, SSRv, 120, 95
Röpke, F. K., Kromer, M., Seitenzahl, I. R., et al. 2012, ApJL, 750, L19
Ryder, S. D., Alsaberi, R. Z. E., Anderson, G., et al. 2022, ATel, 15687, 1
Sai, H., Wang, X., Elias-Rosa, N., et al. 2022, MNRAS, 514, 3541
Sand, D. J., Amaro, R. C., Moe, M., et al. 2019, ApJL, 877, L4
Sand, D. J., Graham, M. L., Botyánszki, J., et al. 2018, ApJ, 863, 24
Sand, D. J., Sarbadhicary, S. K., Pellegrino, C., et al. 2021, ApJ, 922, 21
Sault, R. J., Teuben, P. J., & Wright, M. C. H. 1995, in ASP Conf. Ser. 77, Astronomical Data Analysis Software and Systems IV, ed. R. A. Shaw, H. E. Payne, & J. J. E. Hayes (San Francisco, CA: ASP), 433
Savitzky, A., & Golay, M. J. E. 1964, AnaCh, 36, 1627
Schlafly, E. F., & Finkbeiner, D. P. 2011, ApJ, 737, 103
Schlafly, E. F., Finkbeiner, D. P., Schlegel, D. J., et al. 2010, ApJ, 725, 1175
Schlawin, E., Herter, T. L., Henderson, C., et al. 2014, Proc. SPIE, 9147, 91472H
Science Software Branch at STScI, 2012 PyRAF: Python alternative for IRAF, Astrophysics Source Code Library, record ascl:1207.011
Seaquist, E. R., & Taylor, A. R. 1990, ApJ, 349, 313
Seitenzahl, I. R., Ciaraldi-Schoolmann, F., Röpke, F. K., et al. 2013, MNRAS, 429, 1156
Shappee, B. J., Holoien, T. W. S., Drout, M. R., et al. 2019, ApJ, 870, 13
Shen, K. J., Blondin, S., Kasen, D., et al. 2021a, ApJL, 909, L18
Shen, K. J., Boos, S. J., Townsley, D. M., & Kasen, D. 2021b, ApJ, 922, 68
Shen, K. J., Kasen, D., Weinberg, N. N., Bildsten, L., & Scannapieco, E. 2010, ApJ, 715, 767
Shingles, L., Smith, K. W., Young, D. R., et al. 2021, TNSAN, 7, 1
Siebert, M. R., Foley, R. J., Jones, D. O., et al. 2019, MNRAS, 486, 5785
Silverman, J. M., & Filippenko, A. V. 2012, MNRAS, 425, 1917
Silverman, J. M., Vinkó, J., Marion, G. H., et al. 2015, MNRAS, 451, 1973
Sim, S. A., Fink, M., Kromer, M., et al. 2012, MNRAS, 420, 3003
Smartt, S. J., Valenti, S., Fraser, M., et al. 2015, A&A, 579, A40
Smith, K. W., Smartt, S. J., Young, D. R., et al. 2020, PASP, 132, 085002
Smith, M. P., Nordsieck, K. H., Burgh, E. B., et al. 2006, Proc. SPIE, 6269, 62692A
Srivastav, S., Anupama, G. C., Sahu, D. K., & Ravikumar, C. D. 2017, MNRAS, 466, 2436
Srivastav, S., Smartt, S. J., Huber, M. E., et al. 2023, ApJL, 943, L20
Stevenson, K. B., Bean, J. L., Seifahrt, A., et al. 2016, ApJ, 817, 141
Stritzinger, M., & Leibundgut, B. 2005, A&A, 431, 423
Stritzinger, M., Leibundgut, B., Walch, S., & Contardo, G. 2006, A&A, 450, 241
Sullivan, M., Le Borgne, D., Pritchet, C. J., et al. 2006, ApJ, 648, 868
Suntzeff, N. B. 1996, in IAU Colloq. 145, Supernovae and Supernova Remnants, ed. R. McCray & Z. Wang (Cambridge: Cambridge Univ. Press), 41
Tartaglia, L., Sand, D. J., Valenti, S., et al. 2018, ApJ, 853, 62
Taubenberger, S., Hachinger, S., Pignata, G., et al. 2008, MNRAS, 385, 75
Thomas, R. C., Aldering, G., Antilogus, P., et al. 2011, ApJ, 743, 27
Tinyanont, S., Foley, R. J., Taggart, K., et al. 2023, arXiv:2309.07102
Tody, D. 1986, Proc. SPIE, 627, 733
Tonry, J. L., Denneau, L., Heinze, A. N., et al. 2018, PASP, 130, 064505
Torres, S., Briceño, C., & Quint, B. 2017, Goodman HTS Pipeline Documentation 1.3.6., https://soardocs.readthedocs.io/projects/goodman-pipeline/
Tran, D., Tuttle, S., Mckay, M., Kadlec, K., & Sayres, C. 2019, AAS Meeting, 233, 146.07
Tucker, M. A., Shappee, B. J., Huber, M. E., et al. 2022, PASP, 134, 124502
Tully, R. B., Courtois, H. M., & Sorce, J. G. 2016, AJ, 152, 50
Turatto, M., Benetti, S., Cappellaro, E., et al. 1996, MNRAS, 283, 1
Vacca, W. D., Cushing, M. C., & Rayner, J. T. 2003, PASP, 115, 389
Valenti, S., Howell, D. A., Stritzinger, M. D., et al. 2016, MNRAS, 459, 3939
Valenti, S., Sand, D., Pastorello, A., et al. 2014, MNRAS, 438, L101
Vallely, P. J., Fausnaugh, M., Jha, S. W., et al. 2019, MNRAS, 487, 2372
Virtanen, P., Gommers, R., Oliphant, T. E., et al. 2020, NatMe, 17, 261

Wang, Q., Rest, A., Dimitriadis, G., et al. 2023, arXiv:2305.03779
Wang, X., Filippenko, A. V., Ganeshalingam, M., et al. 2009, ApJL, 699, L139
Wells, D. C. 1985, in Data Analysis in Astronomy, ed. V. di Gesu et al. (New York: Plenum Press), 195
Wilson, J. C., Henderson, C. P., Herter, T. L., et al. 2004, Proc. SPIE, 5492, 1295
Wyatt, S. D., Sand, D. J., Hsiao, E. Y., et al. 2021, ApJ, 914, 57
Yang, Y., Hoeflich, P., Baade, D., et al. 2020, ApJ, 902, 46
Yaron, O., & Gal-Yam, A. 2012, PASP, 124, 668
Zheng, W., Kelly, P. L., & Filippenko, A. V. 2017, ApJ, 848, 66
Zheng, W., Kelly, P. L., & Filippenko, A. V. 2018, ApJ, 858, 104